

GIPC: Fast and stable Gauss-Newton optimization of IPC barrier energy

KEMENG HUANG, The University of Hong Kong, TransGP, Hong Kong
 FLOYD M. CHITALU*, The University of Hong Kong, Hong Kong
 HUANCHENG LIN, TransGP, The University of Hong Kong, Hong Kong
 TAKU KOMURA, The University of Hong Kong, TransGP, Hong Kong



Fig. 1. We offer a robust method enabling simultaneous construction and projection of approximated IPC barrier Hessians to positive semi-definite state for faster implicit time integration. A multilayered cloth animation is shown, where contacts are resolved using our method, which ensures fast convergence rates without numerical eigendecompositions of local barrier Hessians.

Barrier functions are crucial for maintaining an intersection and inversion free simulation trajectory but existing methods which directly use distance can restrict implementation design and performance. We present an approach to rewriting the barrier function for arriving at an efficient and robust approximation of its Hessian. The key idea is to formulate a simplicial geometric measure of contact using mesh boundary elements, from which analytic eigensystems are derived and enhanced with filtering and stiffening terms that ensure robustness with respect to the convergence of a Project-Newton solver. A further advantage of our rewriting of the barrier function is that it naturally caters to the notorious case of nearly-parallel edge-edge contacts for which we also present a novel analytic eigensystem. Our approach is thus well suited for standard second order unconstrained optimization strategies for resolving contacts, minimizing nonlinear non-convex functions where the Hessian may be indefinite. The efficiency of our eigensystems alone yields a $3\times$ speedup over the standard IPC barrier formulation. We further apply our analytic proxy eigensystems to produce an entirely GPU-based implementation of IPC with significant further acceleration.

CCS Concepts: • **Computing methodologies** → **Physical simulation; Collision detection; Massively parallel algorithms.**

Additional Key Words and Phrases: IPC, Barrier Hessian, Eigen Analysis, GPU

*Currently unaffiliated. Was at The University of Hong Kong while contributing to this work.

Authors' addresses: **Kemeng Huang**, kmhuang@connect.hku.hk, kmhuang819@gmail.com, The University of Hong Kong, TransGP, Hong Kong; **Floyd M. Chitalu**, floyd.m.chitalu@gmail.com, The University of Hong Kong, Hong Kong; **Huancheng Lin**, lamws@connect.hku.hk, TransGP, The University of Hong Kong, Hong Kong; **Taku Komura**, taku@cs.hku.hk, The University of Hong Kong, TransGP, Hong Kong.

1 INTRODUCTION

Incremental Potential Contact (IPC) [Li et al. 2020a] is the state-of-the-art for simulating intersection and inversion free updates using implicit integration with large time steps. The main idea of IPC is to formulate non-penetration constraints of mesh boundary elements using distances for constructing a simulator with non-penetration guarantees. These *unsigned* distances are inputs to barrier potentials representing the contact constraints added to the global potential function that is minimized during the updates.

However, physical simulation with robust contact dynamics remains difficult to optimize numerically due to the occurrence of nonconvex local energy landscapes. In particular, second order Newton methods can diverge or stall when the global energy Hessian is indefinite by containing negative eigenvalues [Nocedal and Wright 2006]. Of particular interest is the Projected Newton (PN) method that projects local energy Hessians to the positive semi-definite (PSD) cone prior to assembly of the global Hessian (see e.g. Teran et al. [2005] and Smith et al. [2019]). PN is especially relevant since IPC barrier functions produce locally indefinite Hessians with unknown conditions under which this indefiniteness occurs [Andrews et al. 2022].

Numerical eigendecomposition of the IPC barrier Hessian is the primary solution available to address indefiniteness when using the PN method, which on the other hand hinders the acceleration of the IPC runtime. Numerical eigendecomposition requires iterative computation which is rather slow and also difficult to parallelize on the GPU. As a result, existing massively parallel implementations

of IPC require passing the data between the CPU and GPU, which adds extra overhead to the system.

Analytic eigenanalysis, which is often applied in the simulation of deformable objects, can be an alternative for systematically projecting Hessian to PSD. Indeed, in a recent analysis of penalty-based collision energies [Shi and Kim 2023], closed-form eigensystems were proposed for both signed and unsigned barrier energies, aiming to circumvent numerical eigendecomposition. Nevertheless, this approach encounters severe convergence problems due to the lack of further consideration of nearly parallel edge-edge contacts (see [Li et al. 2020a] for details) and the vanishing displacement problem that we encounter when simulating relatively stiff materials, where the contact primitives get trapped in configurations with minuscule distances, limiting their effectiveness. At such configurations, the second-order derivative of the barrier energy increases rapidly compared to the corresponding first-order derivative, resulting in stalled displacements during Newton iterations.

In this paper, we propose a novel IPC framework that is based on a revised barrier function that forms a Gauss-Newton solver which overcomes the issues faced by existing approaches. We revisit the log barrier function of IPC, augmenting its definition to arrive at an approximate Hessian, where the eigensystem is derived and evaluated analytically for amortizing the cost of assembly and PSD projection. The resulting expressions apply to all configurations of contact (*i.e.* *point-edge*, *point-triangle* etc.), where we also present a novel analytic eigensystem for the notorious nearly-parallel *edge-edge* case. Following our analysis to tackle issues that relate to vanishing displacements, we propose a method for further enhancing the eigensystem of our approximated Hessian to exhibit robust behavior when dealing with distances close to zero. This method involves applying eigenvalue filtering before computing search directions and elevating the barrier profile by steepening its gradient.

Our method provides up to $3\times$ speedup over the distance based formulation of full-space IPC, which is significant given that a few minutes’ worth of simulation typically requires tens of hours to compute and that we obtain visually matching results. We separately demonstrate the flexibility of our analytic eigensystems by engineering a massively parallel implementation of IPC running *entirely* on the GPU (since we bypass need for numerical eigendecompositions) to achieve significant speedups over the publicly-available CPU implementation of Li et al. [2020a]. Within this system, we also apply a matrix-free Preconditioned Conjugate Gradient solver (PCG) with a carefully designed preconditioner that is amenable to GPU data-parallelism for further accelerating nonlinear optimization with Newton’s method. We also demonstrate that by using PCG with a relatively low tolerance (*e.g.* $1e-4$), our system can achieve results that are comparable to a direct solver within Newton’s method.

A summary of our contributions is as follows:

- A formulation of the IPC barrier function to allow efficient Hessian approximations for optimization, which gives local search directions that are aligned with the contact normal. We combined this with our solution to the problem of vanishing displacements for improving convergence of during IPC optimization (§ 5).

- A novel construction of the contact constraint Jacobian from which we measure penetration state. This Jacobian can be extended to handle near-parallel edge-edge cases, enabling approximated eigenanalysis in such scenarios.
- A new mollified barrier function expressed in terms of our constraint Jacobian (§ 6), where we provide analytic eigensystems of its approximate Hessian for fast and robust minimization (§ 6.2).
- A detailed analysis showing that by using a relatively large tolerance, PCG can still efficiently achieve accurate results in nonlinear optimization while using Newton’s method.
- The first full-GPU implementation of IPC, without sacrificing accuracy, that is combined with extensive and rigorous comparisons.

2 RELATED WORK

In this section, we review collision detection and response methods covering IPC, eigenanalysis techniques and GPU accelerated simulation of deformable objects.

Collision Detection. Culling techniques based on spatial hashing [Pabst et al. 2010; Tang et al. 2018a,b] and Bounding Volume Hierarchies (BVH) [Ericson 2005] are the basis for accelerating the collision processing with deformable objects (*i.e.* the broad/mid-phase). A popular representation is the linear-BVH (LBVH) [Lauterbach et al. 2009] which reduces standard construction to a sorting problem by using spatial Morton codes and with several extensions [Apetrei 2014; Chitalu et al. 2020; Karras 2012; Wang et al. 2018]. We refer readers to Meister et al. [2021] for a review of recent developments in acceleration structures.

Continuous Collision Detection (CCD) also plays a vital role in the IPC algorithm and represents part of the narrow-phase: CCD [Provot 1997a; Wang et al. 2021] calculates the maximum feasible steps, thereby preventing inter-penetration during line search with simulations involving implicit time integration. We adopt additive CCD (ACCD) [Li et al. 2021], a numerically stable scheme to iteratively accumulate a lower-bound to convergence-time of impact before collision, which improves efficiency in our parallel implementation on the GPU.

Collision Response. When simulating the contact with deformable objects, the next state must be computed such that all the penetrations are resolved. Methods based on impulse computation [Bridson et al. 2002; Sifakis et al. 2008], impact zone methods [Harmon et al. 2008; Provot 1997b] and constraint solvers [Kaufman et al. 2008; Li et al. 2015; Otaduy et al. 2009] are proposed. Earlier works are based on iterative solvers that resolve collisions by local adjustments [Bridson et al. 2002; Harmon et al. 2008; Provot 1997b]. Such local adjustment can result in adding energy into the system, thus potentially causing instability as a simulation proceeds.

Constraint-based methods describe the combinatorial nature of all possible contact states [Li et al. 2015; Macklin et al. 2019; Otaduy et al. 2009; Verschoor and Jalba 2019]. For example, Otaduy et al. [2009] propose an implicit Linear Complementarity Problem (LCP) based approach that globally resolves the constraints. Li et al. [2015]

present an efficient gradient projection method for computing contact responses by decoupling constraints, while Verschoor and Jalba [2019] tackle the contact problem by directly solving a Mixed LCP (MLCP) and omitting the construction of an LCP matrix. These methods may also make use of signed distance functions (SDF) or their approximations for constructing the constraints. The linearized constraints can be invalidated when the output displacement of the nodes are large [Erleben 2018]. To cope with these issues of SDFs, Li et al. [2020a] instead use unsigned distances which then parameterize barrier potentials that are added to a global objective function resulting in an unconstrained optimization problem of contact. We follow a similar path but address the computational challenge of deriving and simulating with a fast and robust Gauss-Newton approximation scheme that remains efficient with a large number of collision stencils.

Alternatively, volume-based approaches are proposed [Allard et al. 2010; Jiang et al. 2017; Müller et al. 2015; Sifakis et al. 2008] where constraints based on the open-space between the collision pairs are imposed. Müller et al. [2015] pre-compute a volumetric mesh in the open-space and impose positive volume constraints. Jiang et al. [2017] propose a similar shape editing framework to avoid self-penetration. These approaches are only valid when the configuration does not change significantly over time; otherwise an expensive re-meshing process is needed. Sifakis et al. [2008] (see also [Kane et al. 1999]) construct tetrahedra between the colliding pairs every frame and preserve their volume to avoid penetration, where artificial ghost contact forces may appear when sheared to give false positives due to rotations. Our method resembles Sifakis et al. [2008] but we eliminate influence of extraneous rotation by measuring volume via a equivalent strain-like metric that is invariant to such rotations.

Incremental Potential Contact. IPC is proposed by Li et al. [2020a] as a variational method (i.e. formulates a nonlinear system that is solved as an optimization problem) based on Kane et al. [2000]’s incremental potential formulation to update a physical system while ensuring an intersection- and inversion-free simulation trajectory over the duration of the timestep. It has been extended to globally injective 3D shape deformation [Fang et al. 2021], intersection-free rigid body dynamics [Ferguson et al. 2021; Lan et al. 2022a] and simulation of co-dimensional objects [Li et al. 2021]. Unfortunately, IPC has a high computational cost, which may at-times require hundreds-of-seconds to compute one time step [Li et al. 2020a]. Lan et al. [2021] propose Medial-IPC to accelerate the standard model of IPC by using a reduced model to represent the object. Significant speed up is achieved by simulating with less collision pairs in the reduced search space but details of the geometric deformation are lost. Lan et al. [2022b] combine IPC with Projective Dynamics (PD) to implement a full-space penetration-free simulation on GPU, replacing IPC distance-barrier energy with a formulation based on projected target-positions for their barrier constraint. Their framework is efficient but details of deformation are still lost compared with full-space IPC using finite-elements because PD does not guarantee complete physical accuracy and it is also sensitive to time-step size while our approach is practically unaffected (see § 8, Fig. 14).

Eigen Analysis for Energy Minimization. Minimizing contact constrained energies for physical problems is at the core of robust simulations involving elastic body dynamics. Classic 2nd order Newton methods [Nocedal and Wright 2006] can diverge or stall when the energy Hessian is indefinite by containing negative eigenvalues - thus projection to positive semi-definite state is required. For isotropic and anisotropic finite element (FE) energy Hessians, Smith et al. [2019] and Kim et al. [2019] (see also [Kim 2020; Lin et al. 2022; Panetta 2020; Smith et al. 2018]) present analytic expressions for the eigensystems of a wide range of distortion energies. Inline with the analyses of Kim et al. [2019] and Shi and Kim [2023], we extend and rewrite the barrier function to derive analytic eigensystems of its approximate Hessian for a fast and robust Gauss Newton optimization.

GPU optimization. The GPU optimization of physical simulation is sought for accelerating high-quality and computationally demanding animations [Lauterbach et al. 2010; Li et al. 2020c; Müller et al. 2003; Tang et al. 2016, 2018b; Wang 2021]. For deformable objects, researchers have considered accelerating collision response based on zone impacts [Harmon et al. 2008] on the GPU (see e.g. Tang et al. [2018b] and Li et al. [2020c]), while others (e.g. Chitalu et al. [2020]; Lauterbach et al. [2010]) accelerate proximity queries. Parallel techniques like Wang [2021] also simulate sub-millimeter level cloth deformation with regular grids fitted to the garment.

In general, GPU parallelism has been under-utilized for optimizing IPC and its variants. The Affine Body Dynamics (ABD) method [Lan et al. 2022a] is presented as a data-parallel GPU method but a hybrid scheme is described, where e.g. linear system solves are computed on the CPU. Medial IPC [Lan et al. 2021] also partially adopts the GPU acceleration, e.g. for vertex updates through time integration, but a significant portion of computation is still executed on the CPU - such as eigendecomposition, projection and construction of barrier Hessians, as well as solving of large linear systems which we instead compute with a novel data-parallel conjugate-gradient algorithm that scales optimally (cf. § 7).

3 BACKGROUND AND PRELIMINARIES

3.1 IPC optimization and barrier functions

IPC optimization [Li et al. 2020a] is about finding a minimiser

$$\mathbf{x}^{t+\Delta t} \approx \arg \min_{\mathbf{x} \in \mathbb{R}^{3n}} \mathcal{I}(\mathbf{x}), \quad (1)$$

representing the new state of a contact-constrained physical system over a period Δt from time t . This new state is the minimiser of a global potential $\mathcal{I}(\mathbf{x})$, where this potential¹ is defined by the total momentum, elastic, barrier, friction and other (e.g. external loading) terms for n vertex locations in 3-dimensional space stored in vector \mathbf{x} . To do this, an iterated approximation and stepping scheme is applied with local (quadratic) approximation of the potential

$$\mathcal{I}_i(\mathbf{x}) = \mathcal{I}(\mathbf{x}_i) + (\mathbf{x} - \mathbf{x}_i)^T \nabla \mathcal{I}(\mathbf{x}_i) + \frac{1}{2} (\mathbf{x} - \mathbf{x}_i)^T \nabla^2 \mathcal{I}(\mathbf{x}_i) (\mathbf{x} - \mathbf{x}_i). \quad (2)$$

¹The global potential function $\mathcal{I}(\mathbf{x})$ is in general non-convex, which implies that numerical methods like PN cannot guarantee a global minimum, meaning that a local minimum is often reached instead as an *approximation* of the true solution.

For each iteration i , the terms in Eq. (2) are evaluated: A linear solve $\nabla^2 I(\mathbf{x}_i) \cdot \mathbf{d} = -\nabla I(\mathbf{x}_i)$ determines the stationary point $\mathbf{x}_i^* = \arg \min_{\mathbf{x}} I_i(\mathbf{x})$, where $\nabla^2 I(\mathbf{x}_i)$ is symmetric and must be positive definite. The solution $\mathbf{d} = \mathbf{x}_i^* - \mathbf{x}_i$ is the direction of (probable) energy descent with which the new iterate $\mathbf{x}_{i+1} = \mathbf{x}_i + \alpha \mathbf{d}$ is computed, where α is a length parameter from a bounded line-search. The iterated approximation and stepping scheme is terminated when some quantity associated with the stationary point approaches zero - like the solution norm $\|\mathbf{d}\| \leq \varepsilon_d$.

In the remainder, we will focus on the total contribution to the global potential due to barrier energy, which is expressed as a sum over contacts k in a collection C (of *point-triangle*, *point-edge* pairs etc. depending on \mathbf{x})

$$\mathcal{B}(\mathbf{x}) = \sum_{k \in C} b(d_k(\mathbf{x})). \quad (3)$$

(The remaining terms of the global potential $I(\mathbf{x}_i)$ are treated in the same manner as Li et al. [2020a], where we also summarise our treatment of friction in the technical supplement). The local barriers $b(d_k(\mathbf{x}))$ are functions of distance $d_k(\mathbf{x})$ that is evaluated with vertex locations in the stencil of a contact. This distance may be understood as between a point v_p and a triangle $T = (v_{T1}, v_{T2}, v_{T3})$

$$\begin{aligned} \mathcal{D}^{PT} &= \min_{\beta_1, \beta_2} \|v_p - (v_{T1} + \beta_1(v_{T2} - v_{T1}) + \beta_2(v_{T3} - v_{T1}))\| \\ \text{s.t. } &\beta_1 \geq 0, \beta_2 \geq 0, \beta_1 + \beta_2 \leq 1, \end{aligned} \quad (4)$$

and between edges $v_{11} - v_{12}$ and $v_{21} - v_{22}$

$$\begin{aligned} \mathcal{D}^{EE} &= \min_{\gamma_1, \gamma_2} \|v_{11} + \gamma_1(v_{12} - v_{11}) - (v_{21} + \gamma_2(v_{22} - v_{21}))\| \\ \text{s.t. } &0 \leq \gamma_1, \gamma_2 \leq 1. \end{aligned} \quad (5)$$

Then, a given combination of active constraints in Eq. (4) and Eq. (5) will determine the specific distance measure that is used between two potentially intersecting triangles (e.g. *point-edge* distance). This unsigned distance d together with a computational accuracy target \hat{d} then fully parameterizes the smoothly-clamped local barrier potential (cf. Eq. (6) in [Li et al. 2020a])

$$b(d, \hat{d}) = \begin{cases} -(\hat{d} - d)^2 \ln\left(\frac{d}{\hat{d}}\right), & 0 < d < \hat{d} \\ 0 & d \geq \hat{d}. \end{cases} \quad (6)$$

3.2 Minimizing the barrier function

Minimizing Eq. (6) (summed over all contact pairs as in Eq. (3)) together with accompanying terms that define the global potential $I(\mathbf{x})$ gives the solution for contact-constrained dynamics with unconstrained optimization as in Eq. (1), where the order of differentiable energies is C^2 continuous. A solution method for this optimization will employ the approach outlined in § 3.1.

We seek a solution method resembling PN and thereby require forces $\nabla_{\mathbf{x}} b(d, \hat{d}) \Rightarrow \partial b(d, \hat{d}) / \partial \mathbf{x}$ and their Jacobian $\nabla_{\mathbf{x}}^2 b(d, \hat{d}) \Rightarrow \partial^2 b(d, \hat{d}) / \partial \mathbf{x}^2$, where this Jacobian must be PSD. Evaluating this local barrier force Jacobian is relatively straight-forward but *always* indefinite to require numerical eigendecomposition. Li et al. [2020a] as well as Shi and Kim [2023] explore Gauss-Newton approximations to eliminate additional projections but at the cost of reduced solver

convergence rates. We present a novel barrier formulation permitting analytic eigensystems of a comparably approximate Hessian but without reduced convergence rates.

4 MEASURING CONTACT DISTANCE

We re-write the barrier energy in terms of a constraint Jacobian, which is a matrix representing the distortion of a simplex (tetrahedron, triangle or line) defined using vertex locations in the stencil of a contact. We describe in this section our approach to measuring distance using a novel construction of this constraint Jacobian and the contact normal vector from the vertices.

4.1 The gap function

We adopt the following function

$$\begin{aligned} g(\mathbf{x}, \hat{d}) &= \|\mathbf{J}(\mathbf{x}, \hat{d})\mathbf{n}(\mathbf{x})\|_2^2 \\ &\equiv \mathbf{n}(\mathbf{x})^T \mathbf{J}(\mathbf{x}, \hat{d})^T \mathbf{J}(\mathbf{x}, \hat{d}) \mathbf{n}(\mathbf{x}), \end{aligned} \quad (7)$$

as our *gap function* [Andrews et al. 2022] for measuring distance between two contact primitives like a point and a triangle. This function measures distance as a weighted vector-norm with the unit-length normal vector $\mathbf{n}(\mathbf{x}) \in \mathbb{R}^3$ of local contact, where $\mathbf{x} \in \mathbb{R}^{3s}$ is the vector of stacked positions of s vertices ($s = 2, 3$ or 4) defining the simplex. $\mathbf{J}(\mathbf{x}, \hat{d})$ is the constraint Jacobian matrix encoding the directions of local contact forces and torques, which will be defined w.r.t the computational accuracy target \hat{d} : Example constructions are also provided in our technical supplement for reference but we detail our specific implementation in § 4.2.

Eq. (7) is particularly appealing because the eigensystem of an energy expressed solely in its terms can be stated in closed-form (see e.g. Kim et al. [2019]). It is also well suited to the task of measuring the barrier energy in contact configurations that prescribe volume (*point-triangle*, *edge-edge*), area (*point-edge*) or length (*point-point*), which we make use of.

4.2 Evaluating the gap function

Evaluating the gap function in Eq. (7) requires that we compute the Jacobian $\mathbf{J}(\mathbf{x}, \hat{d})$ and normal $\mathbf{n}(\mathbf{x})$ from the vertices of the stencil that have locations \mathbf{x} . We will describe a method to compute $\mathbf{J}(\mathbf{x}, \hat{d})$, which also gives in an implicit expression for $\mathbf{n}(\mathbf{x})$. This implicit expression for $\mathbf{n}(\mathbf{x})$ comes from the observation that the nearest two points between *any* pair of contact primitives (e.g. a point and an edge/triangle from-which we will construct $\mathbf{J}(\mathbf{x}, \hat{d})$) prescribe the normal $\mathbf{n}(\mathbf{x})$ as the nearest direction of contact (cf. Eq. (4) and Eq. (5)). Moreover, we seek a construction of $\mathbf{J}(\mathbf{x}, \hat{d})$ satisfying

$$\mathbf{J}(\mathbf{x}, \hat{d})\mathbf{n}(\mathbf{x}) = \sigma \mathbf{n}(\mathbf{x}), \quad (8)$$

as the zero tangent force condition, where the normal $\mathbf{n}(\mathbf{x})$ is a singular vector of this $\mathbf{J}(\mathbf{x}, \hat{d})$ and $\sigma, 0 \leq \sigma \leq 1$ is the corresponding singular value.

The singular value perspective. Our solution is based on reducing $\mathbf{J}(\mathbf{x}, \hat{d})$ to a diagonal matrix and simplifying $\mathbf{n}(\mathbf{x})$ to a standard basis vector, thereby satisfying Eq. (8) to arrive at an efficient evaluation of $g(\mathbf{x}, \hat{d})$ in Eq. (7). We derive a construction from singular value decomposition (SVD) $\mathbf{J}(\mathbf{x}, \hat{d}) = \mathbf{U}\Sigma\mathbf{V}^T$. From this perspective, we

can view $g(\mathbf{x}, \hat{d})$ as a rotationally invariant measure of the norm of $\mathbf{n}(\mathbf{x})$ when projected into the (squared) principle stretch space Σ^2 , which is crucial for arriving at our solution. Moreover, we have

$$\mathbf{J}(\mathbf{x}, \hat{d})^T \mathbf{J}(\mathbf{x}, \hat{d}) = \left(\mathbf{S}^T \underbrace{\mathbf{R}^T \mathbf{R}}_{\mathbf{I}} \mathbf{S} \right) = \mathbf{S}^2 = \mathbf{V} \Sigma^2 \mathbf{V}^T,$$

with $\mathbf{R}\mathbf{S} := \mathbf{J}(\mathbf{x}, \hat{d})$ as the polar decomposition from which one obtains the rotation $\mathbf{R} = \mathbf{U}\mathbf{V}^T$ for highlighting that $\mathbf{n}(\mathbf{x})$ is merely transformed into the column space of Σ^2 before a dot product in this space. We use this property to define the diagonal *re*-presentation of $\mathbf{J}(\mathbf{x}, \hat{d}) \Rightarrow \Sigma(\mathbf{x}, \hat{d}) \in \mathbb{R}^{m \times m}$ and $\mathbf{n}(\mathbf{x}) \Rightarrow [\text{const}]^T \in \mathbb{R}^m$ satisfying Eq. (8), where $\Sigma(\mathbf{x}, \hat{d})$ will now be evaluated directly from positions $\mathbf{x} \in \mathbb{R}^{3s}$ without any calculation of SVD. The variable $m = 1, 2, 3$ denotes the simplex dimension.

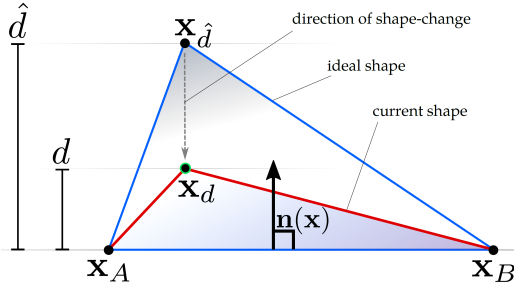


Fig. 2. The ideal shape subtended by vertices \mathbf{x}_A , \mathbf{x}_B and $\mathbf{x}_{\hat{d}}$ is deformed into the current shape (with \mathbf{x}_d instead of $\mathbf{x}_{\hat{d}}$) due to proximal contact where $d < \hat{d}$. Deformation is understood to be in the direction $-\mathbf{n}(\mathbf{x})$, which is opposite to the normal vector that is computed from vertex positions \mathbf{x} in the stencil of the local contact. The positions of the vertices in the stencil here are \mathbf{x}_A , \mathbf{x}_B and \mathbf{x}_d , which come from the mesh boundary elements at the current step. One can always construct the ideal/undeformed shape of the simplex by duplicating a subset of the vertices $\in \mathbf{x}$ and shifting them by an offset $\mathbf{s} = (\hat{d} - d)\mathbf{n}(\mathbf{x})$ from the position of their original copy. Only \mathbf{x}_d is duplicated and shifted by the offset in the example illustrated here. The linear map $\mathbf{J}(\mathbf{x})$ is then a transformation from the ideal to the current shape, which is a pure compression (without shear) due to the uniaxial change-in-shape with \mathbf{s} .

The diagonal Jacobian. To simplify $\mathbf{J}(\mathbf{x}, \hat{d})$ for our intended purpose, we view the simplex as changing shape by deforming along the direction $\mathbf{n}(\mathbf{x})$ from its ideal configuration (see Fig. 2). This means that all but the smallest singular value of $\mathbf{J}(\mathbf{x}, \hat{d})$ are one, which will be

$$f(\mathbf{x}, \hat{d}) = \det(\mathbf{J}(\mathbf{x}, \hat{d})) = \det(\Sigma) = \prod_{i=1}^m \sigma_i = \frac{d(\mathbf{x})}{\hat{d}}, \quad (9)$$

based on the understanding that $\mathbf{J}(\mathbf{x}, \hat{d})$ is a linear map from the ideal to the current shape of the simplex. We also have $\text{diag}(\Sigma) = (\sigma_1, \dots, \sigma_m)$ as the singular values, and $d(\mathbf{x}), 0 < d(\mathbf{x}) < \hat{d}$ as the closest distance between the pair of contact primitives considered.

Eq. (9) follows directly from our construction of the deformed simplex shape which implies *compression* along $-\mathbf{n}(\mathbf{x})$, where the determinant is the ratio of the space (*i.e.* volume, area or length) subtended by the vertex positions of the current shape to those of the ideal shape. This determinant will be equivalent to the distance ratio precisely because we have uniaxial compression to give $\mathbf{J}(\mathbf{x}, \hat{d}) = \mathbf{V}\Sigma\mathbf{V}^T = \Sigma$ since $\mathbf{V} = \mathbf{I}$. The diagonal factor will thus reduce to

$$\Sigma(\mathbf{x}, \hat{d}) = \begin{cases} \begin{bmatrix} 1 & 0 & 0 \\ 0 & 1 & 0 \\ 0 & 0 & f \end{bmatrix} & \text{Point-Triangle and Edge-Edge} \\ \begin{bmatrix} 1 & 0 \\ 0 & f \end{bmatrix} & \text{Point-Edge} \\ [f] & \text{Point-Point,} \end{cases} \quad (10)$$

where f is a substitute for $f(\mathbf{x}, \hat{d})$, and $\sigma_{i=1} \geq \dots \geq \sigma_m$ since the (clamped) barrier function is non-zero when $d(\mathbf{x}) \leq \hat{d}$. We can use this to rewrite Eq. (7) by

$$\bar{g}(\mathbf{x}, \hat{d}) = \mathbf{e}_m^T \Sigma(\mathbf{x}, \hat{d})^T \Sigma(\mathbf{x}, \hat{d}) \mathbf{e}_m = \mathbf{e}_m^T \Sigma^2(\mathbf{x}, \hat{d}) \mathbf{e}_m, \quad (11)$$

where the natural basis vector

$$\mathbf{e}_m = \begin{cases} \begin{bmatrix} 0 \\ 0 \\ 1 \end{bmatrix} & \text{Point-Triangle and Edge-Edge} \\ \begin{bmatrix} 0 \\ 1 \end{bmatrix} & \text{Point-Edge} \\ [1] & \text{Point-Point} \end{cases},$$

then selects for change-of-shape along the contact normal $\mathbf{n}(\mathbf{x}) := \mathbf{e}_m$ with $\mathbf{J}(\mathbf{x}, \hat{d}) := \Sigma(\mathbf{x}, \hat{d})$ to give $g(\mathbf{x}, \hat{d}) = \bar{g}(\mathbf{x}, \hat{d}) = f^2(\mathbf{x}, \hat{d})$, which we use in our implementation².

5 BARRIER FUNCTION

In this section, we describe our barrier function, which is constructed with the gap function described in § 4 for obtaining the analytic eigensystems of the approximate Hessian.

5.1 Notation

For conciseness, we will adopt a convention that functions of one or more variables will be referred to by symbolic name except when first encountered *e.g.* $\mathbf{J}(\mathbf{x}, \hat{d}) \rightarrow \mathbf{J}$. For eigenanalysis, we will write eigenpairs of the barrier Hessian as $(\lambda_i, \mathbf{Q}_i)$, using *eigenmatrix* notation (as in *e.g.* Smith et al. [2019]) instead of the usual notation $(\lambda_i, \mathbf{q}_i)$. This form permits easier derivation of the analytic eigensystems we seek. The usual form is gotten via the relation $\mathbf{q}_i = \text{vec}(\mathbf{Q}_i)$, where the *vectorization* operator $\text{vec}(\cdot)$ denotes a stacking of matrix columns in the simplest case. We also refer readers to the tutorial of Kim and Eberle [2020] for a gist of the tensor notation and analysis methods that we adopt in this paper. A more general treatment of tensor *matricization* and *vectorization* can be found in the work of *e.g.* Kolda and Bader [2009].

²Intuitively, the normal vector has different dimensions (other than just three) because we are measuring distance in the principle-stretch space of \mathbf{J} , which is equivalent to the local space at a contact with the same dimensions as the simplex, m .

5.2 Our barrier, its derivatives and Hessian approximation

We advocate for a barrier potential of the form

$$b(d, \hat{d}) \equiv b(\mathbf{x}, \hat{d}) = -\left(\hat{d}^2 - \hat{d}^2 g(\mathbf{x}, \hat{d})\right)^2 \ln(g(\mathbf{x}, \hat{d})), \quad (12)$$

which is expressed in terms of the gap function g . Using the constraint Jacobian \mathbf{J} as the primary variable that we will be analyzing, the gradient of this energy

$$\frac{\partial b}{\partial \mathbf{x}} = \frac{\partial \mathbf{J}}{\partial \mathbf{x}} : \frac{\partial b}{\partial \mathbf{J}} = \frac{\partial \mathbf{J}}{\partial \mathbf{x}} : \frac{\partial b}{\partial g} \frac{\partial g}{\partial \mathbf{J}} \quad (13)$$

is evaluated by applying the change-of-basis tensor $\partial \mathbf{J} / \partial \mathbf{x}$ via double contraction, with

$$\frac{\partial g}{\partial \mathbf{J}} = 2\mathbf{J}\mathbf{N}, \quad (14)$$

where $\mathbf{N} = \mathbf{n}\mathbf{n}^T$. The second-order derivative (force Jacobian) follows from Eq. (13) by

$$\frac{\partial^2 b}{\partial \mathbf{x}^2} = \frac{\partial \mathbf{J}}{\partial \mathbf{x}} : \frac{\partial^2 b}{\partial \mathbf{J}^2} : \frac{\partial \mathbf{J}}{\partial \mathbf{x}} + \frac{\partial^2 \mathbf{J}}{\partial \mathbf{x}^2} : \frac{\partial b}{\partial \mathbf{J}}, \quad (15)$$

which will be the focus of our analysis.

5.3 Analytic eigensystems of the approximate Hessian

Our goal is to ensure that the barrier Hessian in the first term of Eq. (15)

$$\frac{\partial^2 b}{\partial \mathbf{J}^2} = \frac{\partial b}{\partial g} \frac{\partial^2 g}{\partial \mathbf{J}^2} + \frac{\partial^2 b}{\partial g^2} \left(\frac{\partial g}{\partial \mathbf{J}} \otimes \frac{\partial g}{\partial \mathbf{J}} \right), \quad (16)$$

is PSD but without actually performing *any* numerical eigendecomposition, where \otimes denotes the tensor product operator. The equivalent vectorized form is given by

$$\text{vec} \left(\frac{\partial^2 b}{\partial \mathbf{J}^2} \right) = \frac{\partial b}{\partial g} \text{vec} \left(\frac{\partial^2 g}{\partial \mathbf{J}^2} \right) + \frac{\partial^2 b}{\partial g^2} \text{vec} \left(\frac{\partial g}{\partial \mathbf{J}} \right) \text{vec} \left(\frac{\partial g}{\partial \mathbf{J}} \right)^T, \quad (17)$$

which is what we use to perform eigenanalysis. Applying the analysis of Kim et al. [2019] to Eq. (17), we find that three eigenpairs define our barrier Hessian form (see also Appendix A.2 in [Shi and Kim 2023] for a related approach). The eigenvalues

$$\lambda_1 = 4g \frac{\partial^2 b}{\partial g^2} + 2 \frac{\partial b}{\partial g}, \quad (18)$$

$$\lambda_{2,3} = 2 \frac{\partial b}{\partial g}, \quad (19)$$

are the same for all configurations of contact (*e.g.* edge-edge, point-point etc.) and only the primary *i.e.* λ_1 is ever positive (see technical supplement). We can therefore construct the approximate Hessian of Eq. (12) by

$$\frac{\partial^2 b}{\partial \mathbf{J}^2} \approx \lambda_1 \mathbf{Q}_1 \otimes \mathbf{Q}_1, \quad (20)$$

which is PSD where the eigenmatrix is given by

$$\mathbf{Q}_1 = \frac{1}{\sqrt{g}} \mathbf{J} \mathbf{N}. \quad (21)$$

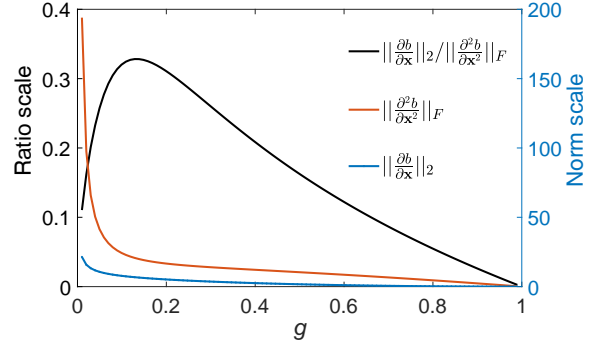


Fig. 3. A plot of the norms of the barrier gradient and Hessian together with their ratio for illustrating the source of vanishing displacements \mathbf{d} as $g \rightarrow 0$. The scalar expressions used to measure the respective norms are described in Appendix B. A threshold of $\hat{d} = 1$ is assumed here to aid visualization.

Neglected terms. Our Hessian approximation is based on the fact that we do not consider the second term of the force Jacobian given in Eq. (15). This omission follows a simplifying assumption on \mathbf{J} , which is that the ideal shape of a simplex is constant w.r.t time to give $\partial^2 \mathbf{J} / \partial \mathbf{x}^2 = 0$ (even though this ideal shape is constructed from $\mathbf{x}(t)$ as shown in Fig. 2). The effect is a cancelling out/removal of the second term in Eq. (15) to arrive at a form resembling the Gauss-Newton approximation of the barrier Hessian form of Li et al. [2020a], which is given by

$$\frac{\partial^2 b}{\partial \mathbf{d}^2} \nabla_{\mathbf{x}} \mathbf{d} (\nabla_{\mathbf{x}} \mathbf{d})^T + \frac{\partial b}{\partial \mathbf{d}} \nabla_{\mathbf{x}}^2 \mathbf{d}, \quad (22)$$

where b is Eq. (6). We share the same subspace of the search direction but not the magnitude of this search direction since our expression in Eq. (18) incorporates information from the omitted second term of Eq. (22). Readers are referred to Appendix A for a more detailed treatment.

5.4 Filtered Hessian

The method presented in § 5.2 and § 5.3 can be used to produce a generally working implementation but is particularly inefficient when the barrier energy is evaluated with a very small distance $d \ll \hat{d}$. Such configurations are rare if simulating with soft elastic materials but occur frequently with high stiffness to affect solver performance. The specific effect is an increase in the number of solver iterations or even convergence failure in the worst case. The source of this problem is the dependence of the barrier function on the log function, which implies that the magnitude of its second-order derivative increases significantly faster than the magnitude of its first-order derivative, to give

$$\|\partial b / \partial \mathbf{x}\|_2 / \|\partial^2 b / \partial \mathbf{x}^2\|_F \rightarrow 0,$$

as shown in Fig. 3. This fact causes the search direction magnitude $\|\mathbf{d}\|_2$ to tend toward zero as $g \rightarrow 0$ since $\mathbf{d} = (\partial^2 b / \partial \mathbf{x}^2)^{-1} \cdot \partial b / \partial \mathbf{x}$, thereby leading to an extremely small step size during optimization with bounded line search when $d \ll \hat{d}$. Li et al. [2020a] multiply each barrier with a dynamically updated global coefficient κ to address

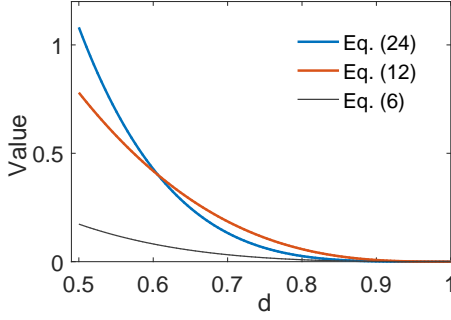


Fig. 4. Barrier function comparison, where a threshold of $\hat{d} = 1$ is assumed to aid visualization. Note that the form $b(d^2, \hat{d}^2)$ is actually used in the source code of Li et al. [2020a] to avoid squared roots, which results in an energy with a profile that is identical to Eq. (12).

this issue. While this suffices when simulating with the full Hessian (Eq. (15)), application is limited if using a GN approximation because the omitted terms of the Hessian incorporate additional components into \mathbf{d} that also work to minimize the energy when $d \ll \hat{d}$ holds³. Furthermore, the magnitude of a search direction calculated with the full hessian can still diminish when evaluating distances near or at a barycentre, which typically occurs when the closest contact-point is near the centroid of a triangle or edge (see supplementary video). We describe in this section an approach to prevent vanishing displacements as $g \rightarrow 0$ by applying a filter directly to Eq. (18) and thereby minimize the barrier energy without reduced convergence rates.

Our solution is to apply a correction on λ_1 , resembling force filtering [Irving et al. 2004] to give

$$\frac{\partial^2 b}{\partial \mathbf{J}^2} \approx \begin{cases} \lambda_1 \mathbf{Q}_1 \otimes \mathbf{Q}_1, & g \geq \epsilon_g \\ \lambda_1^{\text{thr}} \mathbf{Q}_1 \otimes \mathbf{Q}_1, & g < \epsilon_g \end{cases}, \quad (23)$$

as the filtered Hessian that is defined using a proximal limit $\epsilon_g = (d_{\text{thr}}/\hat{d})^2$ via the distance threshold that we set to $d_{\text{thr}} = 0.1\hat{d}$, where λ_1^{thr} is Eq. (18) evaluated at $d = d_{\text{thr}}$. This correction ensures that the magnitude $\|\mathbf{d}\|_2 > 0$ is sufficiently larger than zero for a stable GN optimization. Although effective, this solution has yet one drawback that we must address.

Quadratic stiffening. While Eq. (23) prevents vanishing displacement, the barrier gradient (cf. Eq. (13)) will have insufficient magnitude to get enough repulsion when the adaptive conditioning parameter κ is too small. We propose modifying the barrier function in Eq. (12) to

$$b(d, \hat{d}) = (\hat{d}^2 - \hat{d}^2 g(\mathbf{x}, \hat{d}))^2 \ln^2(g(\mathbf{x}, \hat{d})), \quad (24)$$

where we now use a quadratic log term, which guarantees sufficient force magnitude for minimizing the energy without direct dependence on κ . Stiffening the energy allows for a more locally-adaptive increase in repulsion force, which we found to be sufficient

³It is noteworthy too that these additional components in \mathbf{d} are also associated with a subtle issue of introducing undesirable deviations in motion trajectories over time as shown in Fig. 6.

for eliminating vanishing displacements when combined with our filtered Hessian (Eq. (23)), even when simulating challenging elastic materials with extremely high stiffness as shown in § 8. An illustrative comparison is also provided in Fig. 4. All forms in § 5.2 remain unchanged and therefore the expression of the positive eigenvalue in Eq. (18) and its eigenvector remain the same for evaluating Eq. (23). Eq. (24) is the barrier that we use throughout our implementation.

6 MOLLIFICATION

In this section we describe our approach to handling the notorious case of nearly-parallel edges, which is crucial for minimizing the number of Newton solver iterations and preventing intersections in rare but significant instances. Handling near-parallel edges is especially critical when simulating with accurate Newton tolerance, wherein Newton iteration is highly sensitive to the continuity/smoothness of the energy. Managing near-parallel edges becomes particularly important in such scenarios.

Close-to-parallel *edge-edge* contacts are difficult failure modes because the distance is nonsmooth, where numerical rounding error will also exacerbate barrier energy gradient- and Hessian values. There are two causal problems: The first is that vertices forming any *edge-edge* pair will reduce to a *point-edge* case when the edges are parallel (cf. Fig. 9 in [Li et al. 2020a] and § 7.1 in [Li et al. 2020b]): The consequence is that constraint culling (i.e. dismissal of contact pairs that are farther than \hat{d} apart) may then oscillate between the two possible *point-edge* cases at the parallel configuration during line-search. The effect is long convergence times and even solver divergence because components of the state vector \mathbf{x} that is updated during line-search are determined by contact-force contributions from the three vertices of the *point-edge* case evaluated *prior* to solving the system matrix (see line 8 of Algorithm 1 in [Li et al. 2020a]). The second problem is that the limited precision of floating point numbers prevents a sufficiently accurate calculation of normal vectors (between the edges) to make optimization intractable.

Li et al. [2020a] have addressed these issues by multiplying all *edge-edge* barrier energies by a piecewise polynomial mollifier for smoothening their discontinuous distance gradients at the parallel configuration. This has the effect of coupling all four vertices for assisting line-search. We follow in their steps but tackle the problem from an unconventional-and-yet-intuitive perspective, which is consistent with our approach thus far and permits analytic description of the ensuing approximate Hessian.

6.1 The mollified barrier and its derivatives

Following from § 5.2, we propose

$$e_k(\mathbf{x}, \hat{d}) = \begin{cases} -\frac{1}{\epsilon_x^2} \gamma(\mathbf{x}, \hat{d})^2 + \frac{2}{\epsilon_x} \gamma(\mathbf{x}, \hat{d}), & c < \epsilon_x \\ 1, & c \geq \epsilon_x \end{cases}, \quad (25)$$

as our mollifier for a contact k comprised of nearly-parallel edges. We compute the measure of parallelness $c = \|(\mathbf{x}_{12} - \mathbf{x}_{11}) \times (\mathbf{x}_{22} - \mathbf{x}_{21})\|^2$ from the vertices of the edges (labelled as in Eq. (5)) at the current step; and $\epsilon_x = 10^{-3} \|\bar{\mathbf{x}}_{12} - \bar{\mathbf{x}}_{11}\|^2 \|\bar{\mathbf{x}}_{22} - \bar{\mathbf{x}}_{21}\|^2$ is the tolerance defined using reference positions $\bar{\mathbf{x}}$ from before the first timestep. We introduce the auxiliary function (cf. Eq. (11))

$$\gamma(\mathbf{x}, \hat{d}) = \mathbf{n}_\gamma^T \Sigma^2(\mathbf{x}, \hat{d}) \mathbf{n}_\gamma, \quad (26)$$

for decoupling mollifier terms from our barrier energy to define

$$e_k(\mathbf{x}, \hat{d})b(\mathbf{x}, \hat{d}), \quad (27)$$

as the mollified barrier function. This energy is in-turn evaluated with

$$\mathbf{J} = \Sigma = \begin{bmatrix} 1 & 0 & 0 \\ 0 & \sqrt{c} & 0 \\ 0 & 0 & f \end{bmatrix}, \quad (28)$$

which encodes the state of contact w.r.t the normal (cf. § 4.2) and mollifier. Moreover, we have $\mathbf{n}_\gamma = [0 \ 1 \ 0]^T$ as the vector selecting for the mollification measure \sqrt{c} in \mathbf{J} . We also have $\mathbf{n}_g = \mathbf{e}_m$ as the normal vector that is used to evaluate the barrier term b in Eq. (27), selecting for the distance ratio (cf. § 4.2). Written out explicitly, we have

$$\tilde{b}(\mathbf{x}, \hat{d}) = e_k(\mathbf{x}, \hat{d}) \left(\left(\hat{d}^2 - \hat{d}^2 g(\mathbf{x}, \hat{d}) \right)^2 \ln^2 \left(g(\mathbf{x}, \hat{d}) \right) \right), \quad (29)$$

with $\gamma(\mathbf{x}, \hat{d}) = \|\mathbf{J}(\mathbf{x}, \hat{d})\mathbf{n}_\gamma(\mathbf{x})\|_2^2 = c$, which is the mollified barrier function that we use in our implementation.

Derivatives. Derivatives of the mollified barrier are of the form provided in Eq. (13) and Eq. (15), where

$$\frac{\partial \tilde{b}}{\partial \mathbf{J}} = \frac{\partial \tilde{b}}{\partial \gamma} \frac{\partial \gamma}{\partial \mathbf{J}} + \frac{\partial \tilde{b}}{\partial g} \frac{\partial g}{\partial \mathbf{J}}, \quad (30)$$

and the mollified barrier Hessian is then

$$\begin{aligned} \frac{\partial^2 \tilde{b}}{\partial \mathbf{J}^2} = & \left[\frac{\partial \tilde{b}}{\partial \gamma} \frac{\partial^2 \gamma}{\partial \mathbf{J}^2} + \frac{\partial^2 \tilde{b}}{\partial \gamma^2} \left(\frac{\partial \gamma}{\partial \mathbf{J}} \otimes \frac{\partial \gamma}{\partial \mathbf{J}} \right) \right] + \left[\frac{\partial \tilde{b}}{\partial g} \frac{\partial^2 g}{\partial \mathbf{J}^2} + \frac{\partial^2 \tilde{b}}{\partial g^2} \left(\frac{\partial g}{\partial \mathbf{J}} \otimes \frac{\partial g}{\partial \mathbf{J}} \right) \right] + \\ & \frac{\partial^2 \tilde{b}}{\partial \gamma \partial g} \left(\frac{\partial g}{\partial \mathbf{J}} \otimes \frac{\partial \gamma}{\partial \mathbf{J}} \right) + \frac{\partial^2 \tilde{b}}{\partial g \partial \gamma} \left(\frac{\partial \gamma}{\partial \mathbf{J}} \otimes \frac{\partial g}{\partial \mathbf{J}} \right) \end{aligned} \quad (31)$$

which we use for eigenanalysis (in vectorized form like Eq. (17)).

6.2 Eigenanalysis

Here we describe the analytic eigensystem of our mollified barrier Hessian in Eq. (31), which we analyse on a term-by-term basis (there are four terms).

Eigen values and vectors of the first two terms. The eigenvalues of the first two terms in Eq. (31) each have the form

$$\lambda_{(*)1} = 2 \left(\frac{\partial \tilde{b}}{\partial (*)} + 2(*) \frac{\partial^2 \tilde{b}}{\partial (*)^2} \right),$$

and $\lambda_{(*)2} = \lambda_{(*)3} = 2\partial \tilde{b}/\partial (*)$, where $(*)$ is a substitute for either γ or g in the whole equation. The eigenvalues $\lambda_{\gamma 1}$, $\lambda_{\gamma 2}$ and $\lambda_{\gamma 3}$ are plotted in Fig. 5a and Fig. 5b, which show that $\lambda_{\gamma 1}$ is greater-than zero when $\gamma \lesssim 1/3\epsilon_x$ while $\lambda_{\gamma 2}$ and $\lambda_{\gamma 3}$ are always greater-than or equal-to zero. Likewise, the eigenvalues λ_{g1} , λ_{g2} and λ_{g3} are plotted in Fig. 5c and Fig. 5d, where λ_{g1} is always greater-than or equal-to zero, and λ_{g2} and λ_{g3} are always less-than or equal-to zero.

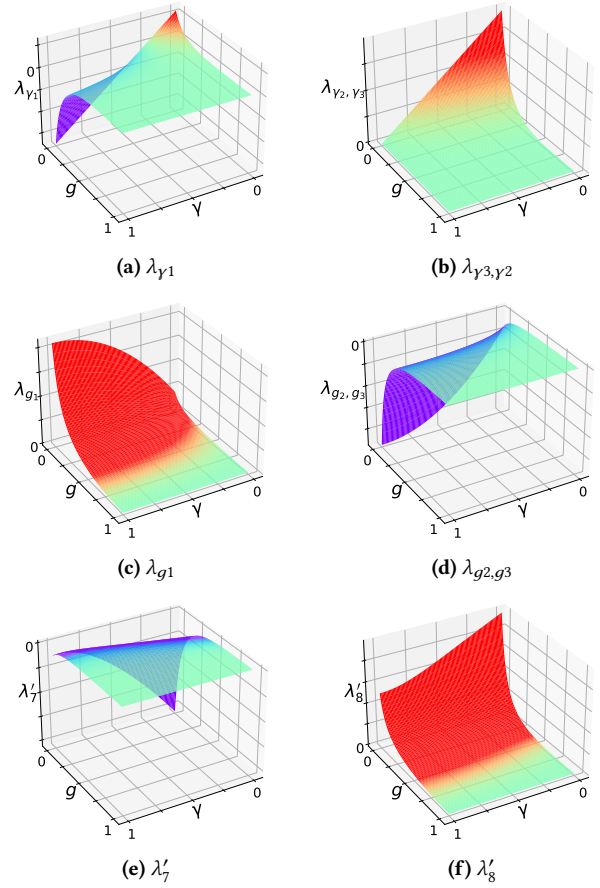


Fig. 5. Plot of the eigenvalues of the approximate mollified Hessian in Eq. (31): Eigenvalues of the first term (Fig. 5a and Fig. 5b); Eigenvalues of the second term (Fig. 5c and Fig. 5d); Eigenvalues due to the third and forth term (Fig. 5e and Fig. 5f).

The corresponding eigenmatrices of $\lambda_{(*)i}$ are (cf. Eq. (12), (15) and (16) respectively in [Kim et al. 2019])

$$\begin{aligned} \mathbf{Q}_{(*)1} &= \mathbf{N}_{(*)}, & \mathbf{Q}_{\gamma 3} &= \begin{bmatrix} 0 & 1 & 0 \\ -1 & 0 & 0 \\ 0 & 0 & 0 \end{bmatrix} \mathbf{N}_\gamma, \\ \mathbf{Q}_{(*)2} &= \begin{bmatrix} 0 & 0 & 0 \\ 0 & 0 & 1 \\ 0 & -1 & 0 \end{bmatrix} \mathbf{N}_{(*)}, & \mathbf{Q}_{g3} &= \begin{bmatrix} 0 & 0 & 1 \\ 0 & 0 & 0 \\ -1 & 0 & 0 \end{bmatrix} \mathbf{N}_g, \end{aligned} \quad (32)$$

where $\mathbf{N}_{(*)} = \mathbf{n}_{(*)} \mathbf{n}_{(*)}^T$. We also have $\mathbf{Q}_{\gamma i} \perp \mathbf{Q}_{\gamma j}$, and $\mathbf{Q}_{gi} \perp \mathbf{Q}_{gj}$, $i \neq j$ with $i, j = 1, 2, 3$, and $\forall_i \mathbf{Q}_{gi} \perp \mathbf{Q}_{\gamma i}$, which means that these eigenmatrices are orthogonal. Readers are referred to our technical supplement for a more detailed derivation.

Third and forth term. Analysis of the last two terms of Eq. (31) will give two eigenpairs

$$\lambda_7 = 2t, \mathbf{Q}_7 = \begin{bmatrix} 0 & 0 & 0 \\ \mathbf{n}_Y^T & & \\ \mathbf{n}_g^T & & \end{bmatrix} \text{ and } \lambda_8 = -2t, \mathbf{Q}_8 = \begin{bmatrix} 0 & 0 & 0 \\ -\mathbf{n}_Y^T & & \\ \mathbf{n}_g^T & & \end{bmatrix}, \quad (33)$$

where $t = \frac{\partial^2 \tilde{b}}{\partial Y \partial g} \cdot \sqrt{c} f$. However, \mathbf{Q}_7 and \mathbf{Q}_8 are not orthogonal to \mathbf{Q}_{Y1} and \mathbf{Q}_{g1} , which means these four bases are not eigenvectors of the complete mollified barrier Hessian expression in Eq. (31).

We resolve this by replacing with (cf. Fig. 5e and Fig. 5f)

$$\lambda'_7 = \frac{\lambda_{Y1}}{2} + \frac{\lambda_{g1}}{2} - p, \mathbf{Q}'_7 = \begin{bmatrix} 0 & 0 & 0 \\ 0 & k_1 & 0 \\ & \mathbf{n}_g^T & \end{bmatrix} \text{ and} \quad (34)$$

$$\lambda'_8 = \frac{\lambda_{Y1}}{2} + \frac{\lambda_{g1}}{2} + p, \mathbf{Q}'_8 = \begin{bmatrix} 0 & 0 & 0 \\ 0 & k_2 & 0 \\ & \mathbf{n}_g^T & \end{bmatrix}, \quad (35)$$

where $k_1 = \frac{\lambda_{Y1} - \lambda_{g1} - 2p}{8t}$, $k_2 = \frac{\lambda_{Y1} - \lambda_{g1} + 2p}{8t}$, and

$$p = \frac{\sqrt{\lambda_{Y1}^2 - 2\lambda_{Y1}\lambda_{g1} + \lambda_{g1}^2 + 64t^2}}{2}.$$

The subspace spanned by \mathbf{Q}'_7 and \mathbf{Q}'_8 now contains \mathbf{Q}_7 , \mathbf{Q}_8 , \mathbf{Q}_{Y1} and \mathbf{Q}_{g1} . This subspace is also orthogonal to \mathbf{Q}_{Y2} , \mathbf{Q}_{Y3} , \mathbf{Q}_{g2} and \mathbf{Q}_{g3} , which is necessary to form a valid eigenspace of the complete mollified barrier Hessian in Eq. (31). The procedure for how we arrive at Eq. (34) and Eq. (35) are summarized in our technical supplement.

The final analytically-projected mollified Hessian is thus

$$\frac{\partial^2 \tilde{b}}{\partial \mathbf{J}^2} = \lambda_{Y2} \mathbf{Q}_{Y2} \otimes \mathbf{Q}_{Y2} + \lambda_{Y3} \mathbf{Q}_{Y3} \otimes \mathbf{Q}_{Y3} + \lambda'_8 \mathbf{Q}'_8 \otimes \mathbf{Q}'_8. \quad (36)$$

We have found a total of six eigenpairs but only three are useful since the eigenvalues λ_{g2} , λ_{g3} and λ'_7 are always less-than or equal-to zero (cf. Fig. 5d and Fig. 5e).

7 IMPLEMENTATION

This section will summarise our implementation of Eq. (1) using a Gauss-Newton solver. We also summarise details of our GPU implementation.

7.1 Overview

The simulation pipeline is summarised in Algo. (1). Given an input triangulated surface mesh, it is first pre-processed (e.g. tetrahedralization, BVH construction *etc.*) during initialization, which is then followed by actual simulation (*i.e.* timestepping via implicit integration). For each timestep, we determine contact pairs by traversing the scene BVHs, querying with all points (to the triangle-BVH) and edges (to the edge-BVH). A pair arises if the distance between the respective primitives (e.g. a point and a triangle) is less than the computational accuracy target \hat{d} . We also set boundary conditions (prescribed positions, velocities and/or force *etc.*, including gravity) before time-stepping the simulation. We follow the standard architecture of a PN solver, with line search and simultaneously

```

init() // Load data, initial conditions  $\mathbf{x}^{t=0}$  etc.
1 for each timestep  $t$  do
2   updateBVHs( $\mathbf{x}^t$ );
3   findContactPairs( $\mathbf{x}^t$ ) // point-triangle pairs etc.
4    $\mathbf{x} \leftarrow \mathbf{x}^t$ ;
5    $I_{\text{prev}} \leftarrow I(\mathbf{x})$ ;
6    $\mathbf{x}_{\text{prev}} \leftarrow \mathbf{x}^t$ ;
7   do
8      $\mathbf{g} \leftarrow \frac{\partial I(\mathbf{x})}{\partial \mathbf{x}}$  // Energy gradient
9      $\mathbb{H} \leftarrow \mathbf{M} + \text{getPSDForceJacobian}\left(\frac{\partial^2 I(\mathbf{x})}{\partial \mathbf{x}^2}\right)$ ;
10     $\mathbb{H}\mathbf{d} = \mathbf{g}$  // PCG solve
11    updateBVHs() // Enlarge BVs with  $\mathbf{d}$ 
12     $\alpha \leftarrow \min(1, \text{maxFeasibleStepSize})$  // Affine CCD
13    do
14       $\mathbf{x} \leftarrow \mathbf{x}_{\text{prev}} + \alpha \mathbf{d}$ ;
15      findContactPairs( $\mathbf{x}$ );
16       $\alpha \leftarrow \frac{\alpha}{2}$ ;
17    while  $I(\mathbf{x}) > I_{\text{prev}}$ ;
18     $\mathbf{x}_{\text{prev}} \leftarrow \mathbf{x}$ ;
19     $I_{\text{prev}} \leftarrow I(\mathbf{x})$ ;
20    Update  $\kappa$ , boundary conditions etc.;
21  while  $\frac{\|\mathbf{d}\|_{\infty}}{\Delta t} \leq \epsilon_d$ ;
22  return  $\mathbf{x}$ ;
23 end

```

Algorithm 1: Implementation overview

```

// Similar steps per contact-pair
1 for each pair  $p$  do
2    $\mathbf{x}_p \leftarrow \text{getLocalContactVertices}(\mathbf{x}, p)$ 
3    $\{\lambda_i, \mathbf{Q}_i\} \leftarrow \text{EvalEigenPairs}(\mathbf{x}_p)$  // e.g. Eq. (18)
4    $\partial^2 b / \partial \mathbf{J}^2 \leftarrow \sum_i \max(\lambda_i^{\text{thr}}, \lambda_i) \mathbf{Q}_i \otimes \mathbf{Q}_i^T$  // e.g. Eq. (23)
5 end

```

Algorithm 2: Steps to evaluate our approximation of Eq. (15)

constructing and projecting each approximate barrier Hessian from our analysis.

7.2 GPU implementation

Existing IPC methods are designed to run either on CPUs (e.g. Ferguson et al. [2021]; Li et al. [2020a]), or via a hybrid combination of the CPU and GPU (e.g. Lan et al. [2022a, 2021]). Hybrid methods are highly efficient but will require marshalling data portions (per Newton iteration) between the CPU and GPU. Our eigenanalysis permits a *completely* GPU based implementation of IPC when combined with recent elastic deformation energies ([Kim 2020; Kim et al. 2019; Lin et al. 2022; Smith et al. 2019] since constructing our barrier Hessian is reduced to evaluating a scaled tensor/outer-product (see Eq. (20) and Algo. (2)). For friction, Li et al. [2020b] describe a method to PSD project the respective friction Hessian, using a 2×2 matrix projection that we also use. The method is relatively straight-forward as it involves simply solving a quadratic problem, which is also efficiently parallelized on the GPU. For a more comprehensive examination of the SPD project of friction Hessian and its impact, readers are referred to the supplemental material.

Data structures. Our BVH representation follows Karras [2012] (although any other suitable method like Chitalu et al. [2020] can be used), which offers a depth-first search (DFS) layout that is ideal for cache-efficient parallel queries using points and edges. BVH traversal will return contact pairs between each query-object (a point or an edge) and the primitive(s) stored in the BVH (triangles or edges). The returned pair(s) for a single query may be further reduced to secondary cases (like a *point-edge* case from *point-triangle*) depending on the number of constraints in the active set (cf. Eq. (4) and Eq. (5)). BVHs are particularly attractive for collision detection on the GPU as they allow for efficient caching with temporal coherence via front-tracking [Wang et al. 2018].

Contact pairs are stored as tuples of vertex indices $\mathbf{t} = (i_0, i_1, i_2, i_3)$ where i_0, \dots, i_3 are these indices. The *type* is then encoded in the sign information of the indices as $[+, +, +, +]$ for *edge-edge*; $[-, +, +, +]$ for *point-triangle*; $[-, +, +, \#]$ for *point-edge*; and $[-, +, \#, \#]$ for *point-point*. The symbol $\#$ is simply a placeholder denoting nullity (i.e. a prescribed value that we can evaluate and compare with). The close-to-parallel *edge-edge* case is encoded with $[+, -, +, +]$ for *edge-edge*; $[-, -, +, -]$ for *point-edge*; and $[-, -, -, -]$ for *point-point*. These tuples are distinguished from normal cases based on the sign information of second index i_1 , which is now negative.

Parallel solver optimizations. Our linear system (cf. Line (10) in Algo. (1)) is solved using modified preconditioned conjugate gradients (modified-PCG) [Baraff and Witkin 1998]. We design the steps of each PCG iteration to bypass full construction of the linear system, using local matrix-vector multiplications to then accumulate results in a global output vector. Briefly, threads (in a CUDA warp) are each mapped to one scalar entry in the local system matrix to then perform multiplication between this scalar and the corresponding component of the input vector (e.g. the vector \mathbf{c} as in Line (5) of the modified-PCG algorithm in [Baraff and Witkin 1998]). The multiplication result computed by each thread is stored in private register memory, which is then accumulated (locally within each CUDA warp) before adding to the global output vector. We provide further implementation detail in our technical supplement, where we also summarise a lock-free ‘warp reduction’ strategy for synchronising register memory access between threads.

Preconditioning of the CG solver. Although our optimized matrix-vector multiplications can significantly reduce the time required for each CG iteration, the total number of CG iterations can still have significant impact on overall performance, especially when dealing with highly stiff elastic materials (e.g. with Young’s Modulus $E = 1e7$). We address this issue by incorporating the state-of-the-art Multilevel Additive Schwarz (MAS) Preconditioner [Wu et al. 2022] for further improving the convergence rate of our matrix-free GPU-CG solver. Notably, this MAS preconditioner will only provide minor improvements in convergence rate when simulating with soft materials due to low conditioning of the system matrix. Executing the MAS preconditioner will also incur additional overhead, which can reduce overall efficiency when compared to a simple block diagonal preconditioner [Tissot 2019] (each block size is 3×3). Therefore, we trial the CG solver with both preconditioners per simulation

and choose the one that is most efficient to take advantage of the benefits of both types of preconditioners.

8 RESULTS AND DISCUSSION

We present our evaluation and results in this section, which are produced on an Ubuntu system with a 16-core Intel Core i9 12900k CPU with 32GB of RAM, and an NVIDIA RTX 4090 GPU with 24GB of RAM. Simulations are updated with the modified-PCG solver [Baraff and Witkin 1998], where we have used a hybrid preconditioner with relative error of $1e-4$ (i.e. to give $\delta_{new} < 1e-4\delta_0$ as the termination condition of PCG). Higher-accuracy thresholds were tested, which we found to have little-to-no further impact on convergence as shown in our technical supplement. The matrix of our linear system (arising at each Newton iteration) is positive-definite due to mass terms added to elastic/barrier Hessian(s). We also compare our system against the CPU implementation of IPC by Li et al. [2020a] with CHOLMOD compiled with intel MKL LAPACK, BLAS and multi-threading for further acceleration. Results are produced with double-precision floating-point numbers, and deformation dynamics use the Stable neo-Hookean energy of Smith et al. [2018], as well as the Baraff-Witkin cloth of Kim [2020] (Fig. 1).

Omitting the second term of the force Jacobian. Fig. 6 shows the effect of evaluating the entire force-Jacobian in Eq. (15) versus evaluating only the first term. A truncation of force-Jacobian terms gives approximate solutions \mathbf{d} , where these solutions remain congruent with the optimal search direction of ‘steepest descent’: Each local approximate solution is aligned with the contact normal vector \mathbf{n} , and barrier energies are minimized precisely by components of the exact solution (computed with the full Hessian) that are parallel-to this normal. Utilizing a normal-aligned search direction can lead to a slightly faster convergence (up to 25%) in nonlinear optimization. However, it does not always guarantee faster convergence, as the local optimal search direction may not necessarily result in the globally optimal convergence rate. This is evident in the results presented in rows Fig. 15 and Fig. 17 of Tab. 5, where the full Hessian method [Li et al. 2020a] achieved a slightly faster convergence.

Approximating the Hessian has further advantages. Using a simple unit-test setup shown in Fig. 7, we also find that solutions computed by evaluating the full Hessian can give inconsistent motion over time, introducing numerical drift-like perturbation of simulation trajectories in the absence of any other external loading besides gravity. Our approximations do not suffer from such drifting. Fig. 8 also shows that our GN approximation generally produces the same visual quality as the reference implementation using the full barrier Hessian in complex simulations. Further demonstrations of the robustness of our method with similar unit tests as Li et al. [2020a] are shown in our supplementary material.

Performance of solver and our analytic eigensystems. Fig. 9 summarises the advantage of our simultaneous construction and projection of barrier Hessians on the GPU when deployed into a full simulation pipeline. We compare with a simulator (‘baseline’), which

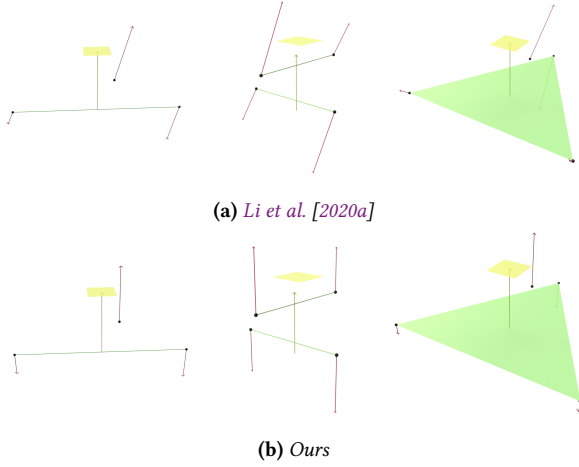


Fig. 6. Evaluating the entire force-Jacobian in Eq. (15) versus evaluating only the first term. The latter (Fig. 6b) restricts the solution vector \mathbf{d} (visualized by the red arrows) to the contact normal direction, and the former (Fig. 6a) is affected by higher order variations between contact pairs due to the nonlinearity of Euclidean distance. The influence of these high-order variations on \mathbf{d} are similarly observed with the distance based formulation of Li et al. [2020a]. Refer to our supplementary video.

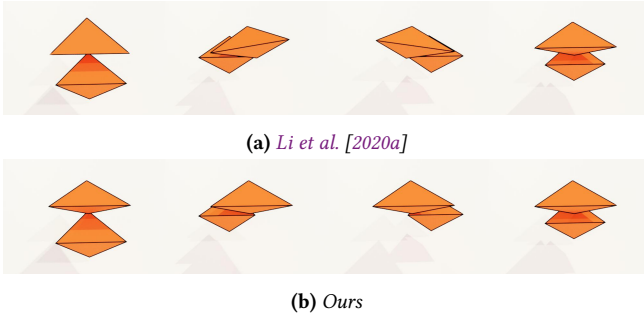


Fig. 7. Validation: Our resting contact is exact. Conversely, using the full Hessian can induce minute variations in motion trajectories subject to the relative positioning between contact pair vertices (point and triangle in this case). Using the full Hessian is only able to achieve artefact-free motion when the local point of contact lies at the barycenter of the test triangle.

performs the same operations as ours except that the barrier Hessians are constructed on the GPU with CPU-side numerical eigendecomposition with Eigen following Medial-IPC⁴ [Lan et al. 2021]. Our

⁴The heterogeneous CPU-GPU implementation in Medial-IPC is driven by the size of the barrier Hessian, where the 12×12 Hessian plays a significant role. Achieving accurate numerical eigendecomposition for such a large Hessian requires numerous iterations with numerical decomposition methods. Unfortunately, these methods are not well-suited for parallelization on GPU. Lower-accuracy decomposition results can lead to substantial deviations and convergence failures in Newton iterations. In contrast, the Eigen library provides reliable numerical results and performs well on CPU, making it more suitable for handling this particular task.

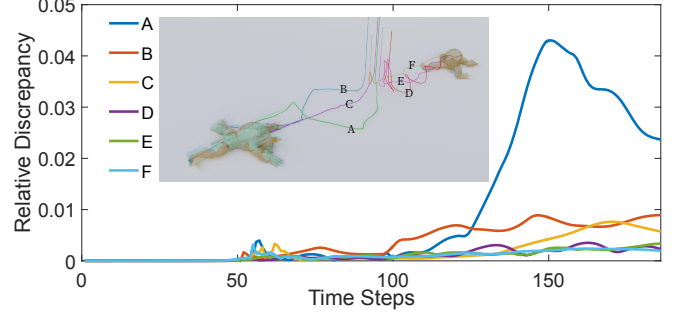


Fig. 8. Comparison of methods: motion discrepancy graphs which are presented comparing a simulation (see inset figure) using the full barrier Hessian versus our approach using only the first term. The curves refer to the discrepancy (measured as mean-squared error) of labelled vertices (A, B, C, D, E and F) on the surface of two Armadillo models. Simulations are run 10 times and averaged per time-step followed by normalization w.r.t. the scene bounding box diagonal of the first time-step. The armadillo models shaded in green denote simulation results evaluated with the full Hessian (i.e. equivalent to Li et al. [2020a]), the orange models represent our results. Transparent curves are thus reference trajectories, while those which are solid are our computed paths.

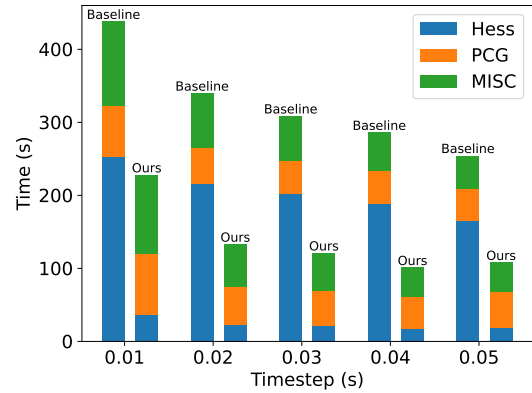


Fig. 9. Impact of eigendecomposition: We use the funnel dolphin example shown in Fig. 14 to demonstrate the time consumption of our IPC barrier Hessian projections on the GPU versus another GPU implementation strategy [Lan et al. 2021] (baseline) that relies on CPU-side numerical eigendecomposition with the Eigen library. 'PCG' is the linear solver and 'Misc' are all other remaining tasks, which are shown here to highlight the time-significance of Hessian construction and projection.

simultaneous construction and projection of barrier Hessians is over 10× faster than the baseline case using the funnel dolphin example (Fig. 14) to give approximately 3× speedup in overall simulation time. Thus, the ease and flexibility with which our analytic eigensystems translate into actual code is also beneficial for improving overall

Table 1. Comparison of time (milliseconds) to construct and project barrier Hessian (Eq. (17)), which has dimensions $\mathbb{R}^{3n \times 3n}$, where n is the number of vertices comprising the contact-pair. Thus, we have $\mathbb{R}^{12 \times 12}$ for point-triangle and edge-edge cases; $\mathbb{R}^{9 \times 9}$ for point-edge; and $\mathbb{R}^{6 \times 6}$ for point-point. The first column shows the number of barrier Hessians. Our analytic eigensystems are faster with upto $7.8\times$ speedup on CPU.

$\partial^2 b / \partial \mathbf{J}^2$		CPU			GPU	
Count	Dims	Eigen	Ours	Speedup	Ours	Speedup
10^7	$\mathbb{R}^{12 \times 12}$	2.42e3	4.95e2	4.88×	9.01e1	5.50×
	$\mathbb{R}^{9 \times 9}$	1.45e3	2.29e2	6.33×	4.10e1	5.58×
	$\mathbb{R}^{6 \times 6}$	4.79e2	9.68e1	4.94×	1.32e1	7.28×
10^6	$\mathbb{R}^{12 \times 12}$	2.42e2	5.01e1	4.82×	9.03	5.54×
	$\mathbb{R}^{9 \times 9}$	1.49e2	2.21e1	6.73×	4.05	5.46×
	$\mathbb{R}^{6 \times 6}$	5.02e1	9.71	5.17×	1.37	7.05×
10^5	$\mathbb{R}^{12 \times 12}$	2.36e1	4.83	4.47×	1.08	5.16×
	$\mathbb{R}^{9 \times 9}$	1.44e1	2.22	6.48×	4.23e-1	5.25×
	$\mathbb{R}^{6 \times 6}$	5.01	6.38e-1	7.86×	1.62e-1	3.92×
10^4	$\mathbb{R}^{12 \times 12}$	2.33	5.22e-1	4.46×	1.76e-1	3.23×
	$\mathbb{R}^{9 \times 9}$	1.50	2.25e-1	6.65×	6.28e-2	3.58×
	$\mathbb{R}^{6 \times 6}$	5.04e-1	7.55e-2	6.67×	2.62e-2	2.87×
10^3	$\mathbb{R}^{12 \times 12}$	2.38e-1	5.57e-2	4.27×	1.65e-1	3.37e-1×
	$\mathbb{R}^{9 \times 9}$	1.55e-1	3.05e-2	5.09×	5.69e-2	5.37e-1×
	$\mathbb{R}^{6 \times 6}$	5.82e-2	1.42e-2	4.08×	2.23e-2	6.37e-1×

data-parallel performance especial when the number of collision pairs is larger (e.g. by $4\times$) than the number of finite elements.

We additionally perform a focused comparison of the time to evaluate our analytic eigensystems versus the time to compute the traditional procedure of constructing and then numerically projecting barrier Hessians with Eigen [Guennebaud et al. 2022]. Elapsed time is measured 1k times to estimate averages. On the CPU we achieve at least $4.0\times$ and up-to $7.8\times$ speedup over Eigen. The GPU implementation of our analytic eigensystems up-to $7.2\times$ faster than our CPU implementation. Refer to Tab. 1. It is worth noting that such an SPD performance problem only arises in a well-optimized GPU IPC framework, where the linear solver and collision detection components are well optimized.

To evaluate the performance improvement due to our fine-grain strategy for parallelizing local matrix-vector multiplications during PCG, we compare with an alternative implementation that directly scales the number of GPU threads by the number of contact pairs and finite elements. That is, computing one local matrix-vector multiplication per GPU thread like Gao et al. [2018]. Our results are shown in Tab. 2, which are based on evaluations using four scenes. Our PCG solver is up-to $4\times$ faster than the baseline reference (averaging $3.97\times$), which leads to an overall $2\times$ speedup in simulation time.

Material stiffness and performance. Fig. 11 and Tab. 3 show the impact of material stiffness on the number of Newton solver iterations, where we compare our method with Li et al. [2020a] and their discussed Gauss-Newton method (cf. Eq. (22)), as well as the recent method of Shi and Kim [2023]. The detailed experimental

Table 2. Comparison of parallel PCG solver time (in seconds). We compare against an implementation where each local/per-Barrier term matrix-vector multiplication (during PCG) is computed by one GPU thread. Table columns are as follows: Total time spent computing linear system (PCG); Miscellaneous simulation tasks (Misc); Total simulation time (TimeTot); total number of conjugate gradient iterations (#cg); Total number of Newton solver iterations (#Newton); Average number of conjugate gradient iterations per Newton solve iteration (#cg per iter). Both methods are tested with the same PCG threshold of $1e-4$.

		PCG	Misc	TimeTot	#cg	#Newton	avg #cg per iter
Fig. 17	Ours	1.18e3	5.83e2	1.76e3	2.66e6	2.19e4	121.1
	Baseline	4.69e3	5.83e2	5.27e3	2.65e6	2.19e4	121.0
	Speedup	3.98×	-	2.99×	-	-	-
Fig. 15	Ours	1.12e3	1.26e3	2.38e3	3.42e6	4.24e4	80.6
	Baseline	4.28e3	1.25e3	5.53e3	3.43e6	4.23e4	81.0
	Speedup	3.82×	-	2.32×	-	-	-
Fig. 18	Ours	3.68e3	2.37e3	6.05e3	9.50e5	1.41e4	67.4
	Baseline	1.51e4	2.37e3	1.75e4	9.54e5	1.41e4	67.7
	Speedup	4.11×	-	2.89×	-	-	-
Fig. 19	Ours	1.25e3	8.80e2	2.13e3	2.10e6	1.72e4	122.1
	Baseline	5.01e3	9.00e3	5.91e3	2.13e6	1.74e4	122.3
	Speedup	4.00×	-	2.77×	-	-	-

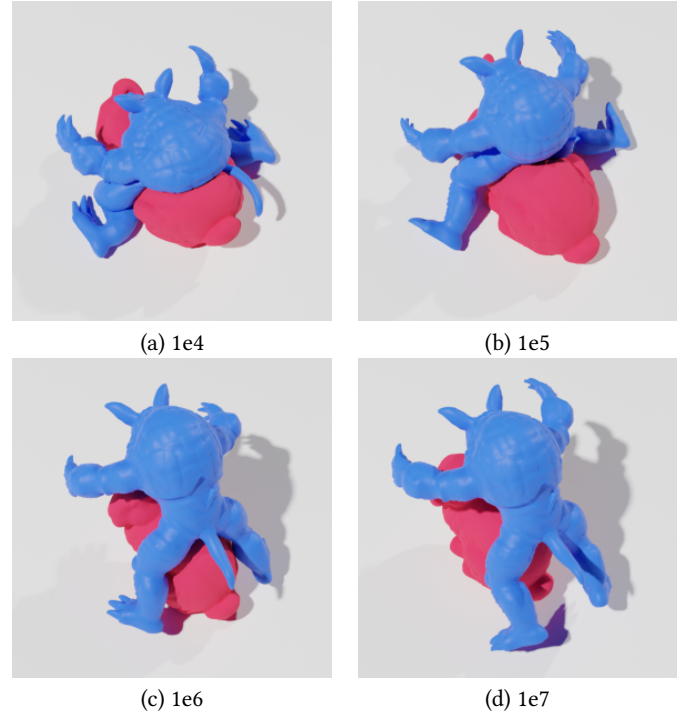


Fig. 10. Simulating with different values for material stiffness (Youngs modulus): Our framework can handle extremely large stiffness simulations efficiently.

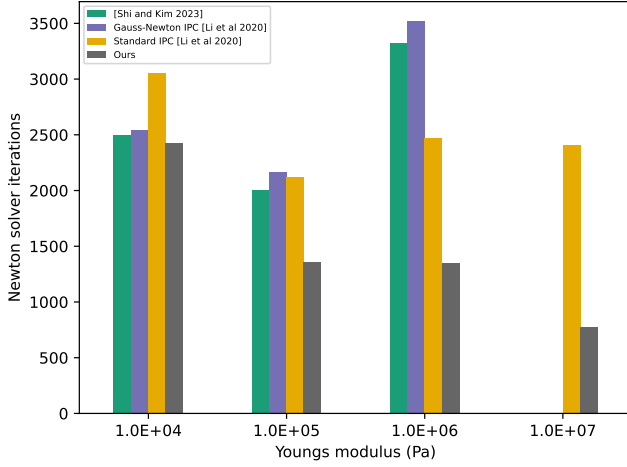


Fig. 11. A plot comparing the number of Newton solver iterations versus material stiffness (GPa). The plotted data (cf. Tab. 3) is obtained from the demos shown in Fig. 10 (a) (b) (c) and (d), respectively. Our implementation requires the least number of iterations for the values of Young modulus tested (up-to $3\times$ less). Thus, our method is more efficient than Li et al. [2020a] as well as Shi and Kim [2023] by overcoming the drawbacks typically associated with a Gauss-Newton approximation of the barrier Hessian like significantly low convergence rates or even failure to converge with highly stiff materials (e.g. $E = 1e7$).

Table 3. A comparison based on the number of Newton solver iterations w.r.t material stiffness (Youngs modulus). See also Fig. 11.

Youngs modulus (Pa)	Method			
	Shi and Kim [2023]	Gauss-Newton IPC	Standard IPC	Ours
1E4	2501	2543	3053	2427
1E5	2006	2162	2123	1358
1E6	3326	3519	2475	1352
1E7	FAIL	FAIL	2412	779

Table 4. A comparison based on the behaviour of the projected-Newton solver, where we measure the number of iterations versus tolerance. See also Fig. 12 for a visualisation.

Tolerance	Method				
	Gauss-Newton IPC	Shi and Kim [2023]	Standard IPC	Ours (without mollifier)	Ours
1E-2	2543	2501	3159	2478	2427
1E-3	4606	4633	5772	4628	4546
1E-4	9206	9186	9300	9186	7441
1E-5	FAIL	FAIL	11123	FAIL	9434
1E-6	FAIL	FAIL	14474	FAIL	12495

settings are provided in row Fig. 10 of Tab. 5, which were utilized for all comparison methods. For the values tested, we find that our method requires the least amount of iterations to converge in every case (up to $3\times$ less), which demonstrates that our combination of projected Hessian approximations with mollification can lead to a more efficient simulator. The method of Shi and Kim [2023] requires a consistently higher number of iterations (up to $2.4\times$ more in our

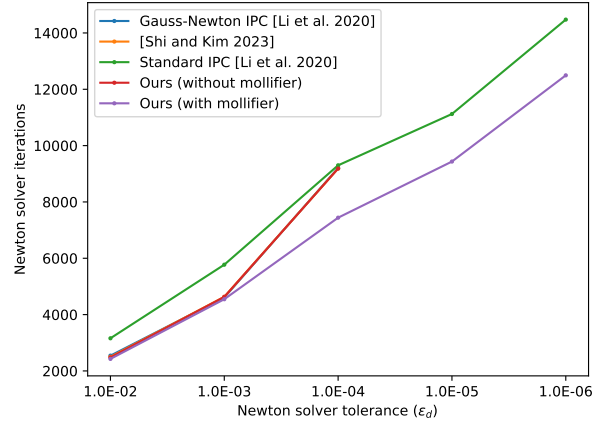


Fig. 12. Comparison of PN solver iteration count versus convergence threshold ϵ_d (scaled by scene bounding box diagonal), where we have used the demo in Fig. 10 (a) to obtain our data for a fair comparison since the Gauss-Newton IPC and the method of Shi and Kim [2023] are susceptible to failure (e.g. when $\epsilon_d = 10^{-5}$ or material is stiff). We compare our analytically projected mollified Hessian in § 6.2 with four alternative implementations to show the practical advantage of our method in improving convergence rates even with small thresholds ϵ_d . The data shown here is also provided in Tab. 4 for reference.

tests) and we found it unable to simulate stiff materials e.g. with $E = 1e7$.

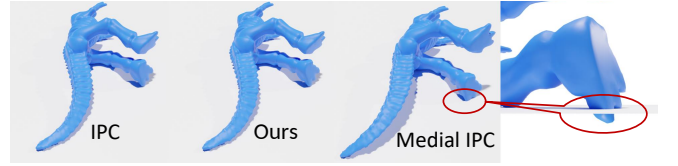


Fig. 13. We compare our GIPC framework with Medial-IPC [Lan et al. 2021]. We use the scene from Medial-IPC’s publicly available source code, which we configure as follows: $\Delta t = 0.02$, $E = 1e3$, $v = 0.35$, $\rho = 2$, which aligns with the default setting of Medial IPC. The solver threshold is set to $\epsilon_d = 1e-2l$ and the distance threshold to $\hat{d} = 1e-3l$, which aligns with the default setting of standard IPC.

Nearly-parallel edges. The significance of our novel analytically projected mollified barrier Hessian is demonstrated with comparison against alternative strategies as shown in Fig. 12 and Tab. 4. The impact of our approach to handling nearly-parallel edge-edge contacts is most observable when simulating with extremely small solver thresholds ϵ_d . Comparing across the spectrum from $\epsilon_d = 10^{-2}$ to $\epsilon_d = 10^{-6}$, we find that our mollifier yields the lowest number of iterations in most settings evaluated. Our improvement is most significant when using extremely small thresholds (e.g. $\epsilon_d = 10^{-5}$ and above), where Gauss-Newton IPC, our approach without mollification and the method of Shi and Kim [2023] fail.



Fig. 14. *Funnel test: From top to bottom we show simulation with varying timestep sizes. The simulation remains both intersection- and inversion-free throughout all time steps.*

Funnel dolphin. We also demonstrate the robustness of our contact resolution with elastic material undergoing severe compression and strong boundary conditions. Repeating Li et al. [2020a]’s funnel test, we pull a elastic material dolphin model through a co-dimensional funnel mesh. Several time step sizes are evaluated ranging from 0.01s to 0.05s with the results shown in Fig. 14. Our simulations remain intersection- and inversion-free across all time-steps, demonstrating the robustness of our method even for relatively large time step sizes.

Medial-IPC. Fig. 13 shows an experimental setup, which we use to compare results with Medial-IPC [Lan et al. 2021] (using their publicly available source code) to evaluate visual quality and performance. Medial-IPC offers a fast reduced simulation framework with GPU optimization but does not resolve contacts exactly due to an inconsistency of medial primitives and deformed vertices positions (see Fig. 13, right). We conducted our performance comparisons with Medial-IPC on Windows because the available implementation of Medial-IPC source code is based on this operating system. It is worth noting too that standard IPC [Li et al. 2020a] runs significantly faster on Linux than on Windows for several reasons (including better support for Intel’s MKL), some of which are unknown. Thus, to ensure a fair comparison with IPC for this experiment, we still run it on Linux with the same the optimizations mentioned for CPU IPC. For performance, we have found our method (average 0.38s/frame) to be 5.2× faster than Medial-IPC *in this setup* (average 2.0s/frame), where we have also found Medial-IPC to be 2.2× faster than standard IPC [Li et al. 2020a] (average 4.3s/frame). Our method is 11.3× faster than standard IPC here, which is generally lower than other results shown in Tab. 5. Such a lower speedup of our method over standard IPC is to be expected however due the relatively low amount of work for GPU parallelism, while the relative stiffness is large.

Overall performance. The overall performance summary of our method is provided in Tab. 5, where we report both CPU [Li et al. 2020a] and GPU (ours) running time. For reference dynamics please see our supplemental video. Our method achieves significant speedup in all cases evaluated. Our GPU method is on average 46.7× faster than the reference CPU implementation. Our lowest speedup is 11.3×, and in the best case we achieve up-to 95.7× faster performance. For reference, the rod twist simulation in Fig. 17 (twisted for 50s) took over 20.3 hours with the CPU implementation, compared to a mere 29.3 minutes with our simulator. To further validate the enhancements brought about by our barrier method, we replicated the scenarios depicted in Fig. 10 and Fig. 14 using CPU-IPC [Li et al. 2020a] alongside our barrier method. Additional details and results can be found in our technical supplement.

The supplementary dressed-actor animation shown in Fig. 1 is modelled with 160k triangles and simulated with the finite element formulation of the Baraff-Witkin model [Kim 2020]. The simulation took 0.09s per Newton iteration using a timestep size of 0.01s, with an average of 25 iterations per timestep to solve fully converged deformation and frictional contact. The whole animation sequence contains 2678 timesteps and is computed within 1.8 hours. The human body motion is from the AMASS dataset [Mahmood et al. 2019]

Differentiable simulation. IPC and its variants [Lan et al. 2021; Li et al. 2020a, 2021] have introduced differentiable contact handling methods. Building upon this foundation, Huang et al. [2022] have developed a differentiable solver based on IPC. However, its performance is hindered by the bottleneck of CPU-IPC, resulting in slow computation times. We here show a material parameter optimization demo by making use of the differentiability of our GPU simulator with a cloth example (see Fig. 16). The apparel in the middle row (blue) shows the forward simulation with a random initial stretch stiffness parameter; the lower row (purple) shows the simulation with optimized stretch stiffness solved with the inverse method of Sifakis et al. [2005] and our barrier gradients, such that it matches the target deformation shown in Fig. 16, top row. Our optimized simulation closely matches the target trajectory. Note that the lower part of the apparel is composed of two layers and thus the deformation due to self-contacts must be also differentiable for the optimization to converge.

While there is still room for further exploration of differentiable simulation techniques, our method brings notable performance advantages to the field. Specifically, our approach introduces a highly efficient GPU IPC framework that ensures intersection-free simulations. As evidenced by our results, this inverse simulation (the cloth is modeled with approximately 15,000 triangles.) was successfully completed in just 200 seconds, encompassing 300 time steps, showcasing the speed and effectiveness of our method.

9 CONCLUSION AND DISCUSSION

We have presented a new barrier function that requires minimal effort to ensure positive semi-definiteness of its approximate Hessian for efficient Gauss-Newton optimization of IPC. Proximal contact is represented as compressive distortion of a simplex, giving rise to the constraint Jacobian from the positions of vertices in the stencil

	v,t,f	ρ, E, ν	\hat{d}, ϵ_d	μ, ϵ_v	$\Delta t, \# \Delta t$	buildCP		buildGH		solve		CCD		#i		misc		timeTot		speedup (gpu vs. cpu)
						cpu	gpu	cpu	gpu	cpu	gpu	cpu	gpu	cpu	gpu	cpu	gpu	cpu	gpu	
Fig. 1	80k, -, 160k	1e2,1e2,0.49	3e-4l, 4e-2l	0.4, 1e-3l	0.01, 2678	-	9.96e2	-	2.70e2	-	4.78e3	-	3.02e2	-	25.1	-	44	-	6.40e3	-
Fig. 15	45k, 133k, 89.9k	1e3,1e4,0.48	1e-3l, 1e-2l	-	0.01, 5k	2.63e4	6.31e2	4.91e3	3.79e2	7.23e4	1.12e3	2.08e4	1.19e2	8.33	8.48	6.27e3	131	1.31e5	2.38e3	55.0x
Fig. 17	53.3k, 202k, 79.8k	1e3,1e4,0.49	1e-3l, 1e-2l	-	0.01, 5k	1.21e4	1.62e2	3.55e3	2.78e2	4.16e4	1.18e3	9.90e2	3.35e1	4.27	4.39	5.83e3	106	7.30e4	1.76e3	41.5x
Fig. 18	518k, 2158k, 562k	1e3,1e4,0.49	3e-4l, 1e-2l	0.2, 1e-3l	0.01, 224	1.17e5	6.70e2	2.75e4	1.56e3	3.75e5	3.68e3	5.77e4	1.01e2	79.4	63.2	1.44e3	39.7	5.79e5	6.05e3	95.7x
Fig. 19	123k, 330k, 211k	1e3,1e4,0.49	4e-4l, 2e-2l	-	0.01, 200	2.66e4	3.94e2	4.16e3	3.93e2	5.98e4	1.25e3	2.02e4	8.97e1	89.9	85.9	1.95e2	3.30	1.11e5	2.13e3	52.1x
Fig. 21	36k, 135k, 46k	1e3,1e4,0.49(body) 1e2,1e2,0.49(cloth)	3e-4l, 1e-2l	0.5, 1e-3l	0.01, 350	6.65e3	1.10e2	1.63e3	1.27e2	1.83e4	2.67e2	2.83e3	1.89e1	48.1	43.2	1.15e2	3.86	2.96e4	5.28e2	56.1x
Fig. 10	32k, 135k, 38k	1e3,1e4,0.49	1e-3l, 1e-2l	-	0.01, 95	6.33e2	8.76	2.97e2	2.28e1	3.39e3	3.60e1	5.41e2	2.86	33.2	25.5	1.93e1	0.68	4.88e3	7.11e1	68.6x
		1e3,1e5,0.49			0.01, 80	4.09e2	3.95	2.05e2	1.25e1	2.32e3	3.92e1	3.58e2	1.35	26.5	17.0	1.81e1	0.40	3.31e3	5.74e1	57.7x
		1e3,1e6,0.49			0.01, 100	4.66e2	3.70	2.39e2	1.22e1	2.74e3	7.63e1	4.04e2	1.24	24.8	13.5	2.14e1	0.66	3.87e3	9.41e1	41.1x
		1e3,1e7,0.49			0.01, 81	4.62e2	2.07	2.33e2	6.97	2.62e3	8.49e1	3.94e2	0.73	29.8	9.61	3.11e1	0.43	3.74e3	9.51e1	39.3x
Fig. 20	77k, 290k, 108k	1e3,1e8,0.40	1e-4l, 1e-2l	1.0, 1e-3l	0.01, 250	6.74e2	5.58	2.28e2	1.67e1	1.98e3	1.15e2	4.35e2	2.08	4.78	3.97	5.30e1	4.64	3.37e3	1.44e2	23.4x
Fig. 13	17k, 56k, 34k	2,1e3,0.35	1e-3l, 1e-2l	-	0.02, 200	2.20e2	3.90	48.1	6.37	3.73e2	5.96e1	2.03e2	2.94	7.61	7.60	1.59e1	3.29	8.60e2	7.61e1	11.3x
Fig. 14	8k, 36k, 10k(dolphin) 30k, -, 60k(funnel)	1e3,1e4,0.40	1e-3l, 1e-2l	-	0.01, 300	2.64e3	7.91e1	5.47e2	2.94e1	3.46e3	6.71e1	2.06e3	1.79e1	22.7	20.9	1.84e2	4.51	8.89e3	1.98e2	44.9x
					0.02, 150	1.62e3	4.27e1	4.27e2	2.23e1	2.55e3	5.31e1	1.36e3	1.25e1	29.6	23.4	1.03e2	3.02	6.06e3	1.33e2	45.3x
					0.03, 100	1.24e3	3.67e1	3.62e2	2.14e1	2.13e3	4.88e1	1.09e3	1.17e1	36.8	29.6	6.82e1	2.31	4.89e3	1.21e2	40.4x
					0.04, 75	9.69e2	2.82e1	3.28e2	1.75e1	1.72e3	4.30e1	8.93e2	1.01e1	38.4	30.5	5.38e1	1.83	3.97e3	1.01e2	39.4x
					0.05, 60	8.86e2	2.85e1	3.13e2	1.49e1	1.59e3	4.56e1	8.28e2	1.05e1	43.6	38.3	4.47e1	1.52	3.66e3	1.01e2	36.2x

Table 5. Performance summary using comparison Li et al. [2020a]. The columns are as follows: number of vertices, including the interior for tetrahedral meshes (v); number of tetrahedra (t); number of surface triangles (f); time step size in seconds (Δt); material density(ρ), Young’s modulus (E) in units of pascals Pa, and Poisson’s ratio (ν); computational accuracy target in meters (\hat{d}) which is set w.r.t. to the scene bounding box diagonal length l ; Newton Solver tolerance threshold (ϵ_d); friction coefficient (μ) and velocity magnitude bound (ϵ_v); Total number of time steps ($\# \Delta t$); Total time to build/find contact pairs (buildCP); Total time to build energy gradients and Hessians for all types (buildGH); Total linear solver time (solve); Total CCD time (CCD); Average number of Newton iterations per time step ($\#i$); Total time for remaining miscellaneous tasks (misc); Total simulation compute time (timeTot); Estimated speedup of GPU implementation (ours) versus CPU (Li et al. [2020a]). All time measurements are presented in seconds.

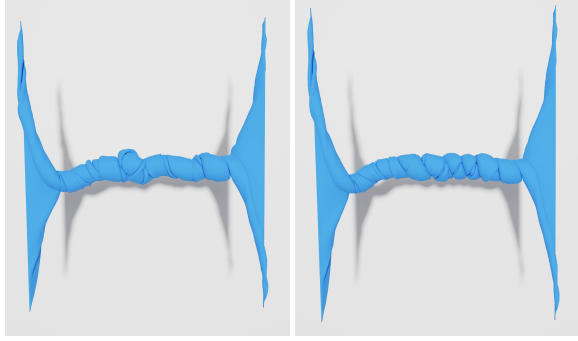


Fig. 15. Twisting cloth: Here we reproduce Li et al. [2020a]’s cloth stress test with extreme twisting of a volumetric mat for 100s.

of a contact pair. This constraint Jacobian is the source of our novel derivation and analysis of the barrier function, enabling closed-form expressions for the eigendecomposition of the approximate Hessian. With the exception of the near-parallel *edge-edge* case, all configurations of contact are found to have the same expressions (three) for their eigensystem. One eigenvalue is always positive (and others are negative) which we use to PSD project the approximate Hessian and define a filtering strategy for improving Gauss-Newton convergence rates.

As an ‘oriented-simplex’ method, our approach is inspired by the idea of constructing deformation gradients [Sifakis and Barbic 2012] with matrices composed of vectors along the edges of a simplex, then inverting one of the matrices and multiplying. This idea is remarkably powerful, enabling stress-like measurement of contact where the gradient of the barrier potential w.r.t the Jacobian $\partial b / \partial \mathbf{J}$ is the linear operator for mapping a normal vector \mathbf{n} in the local

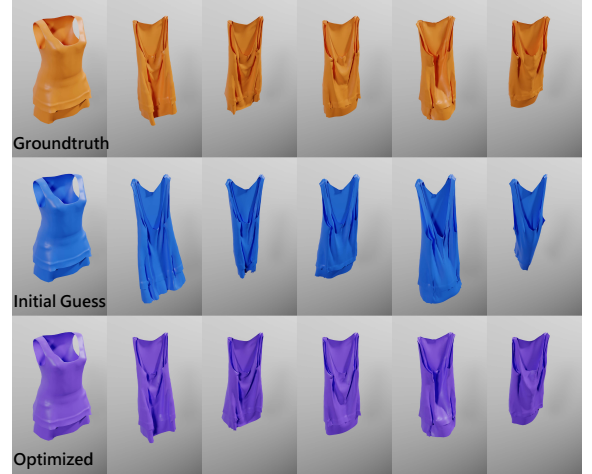


Fig. 16. Differentiable test: We show a simulation with optimized stretch stiffness to match the target trajectory.

space (of a contact) to the force vector $\mathbf{f}_c = -\partial b / \partial \mathbf{x}$ in world space across the surface perpendicular to this \mathbf{n} .

Our constraint Jacobian is related but differs from the deformation gradient in that it is always diagonal, which permits efficient and elegant evaluations of the barrier energy. The resulting construction is free of explicit assemblage (*i.e.* without actual use of vectors along simplex edges, matrix inversions nor multiplications) and naturally extends to our mollification of the barrier function in situations of degenerate near-parallel edges.

Limitations and future work. Despite integrating the state-of-the-art MAS preconditioner [Wu et al. 2022] into our framework, our

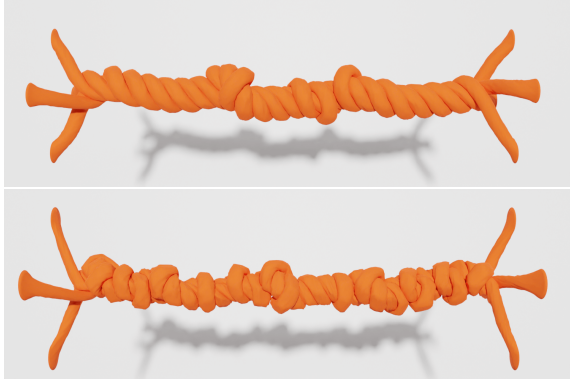


Fig. 17. Rod twist: In this example, we reproduce the rod twisting test.



Fig. 18. Bunny drop: We simulate 27 Stanford Bunny models containing 2158k tetrahedra and a total of 1686k degrees of freedom. Our GPU simulation is over 95 \times than standard IPC [Li et al. 2020a] on the CPU.



Fig. 19. Furry balls: Two soft spheres embellished with protruding soft spikes are dropped to the ground, resulting in intricate collisions between their strands with deformation.

approach can still exhibit reduced speedup as the stiffness of the problem increases (see also Tab. 5, rows of Fig. 10, Fig. 14 and Fig. 20).

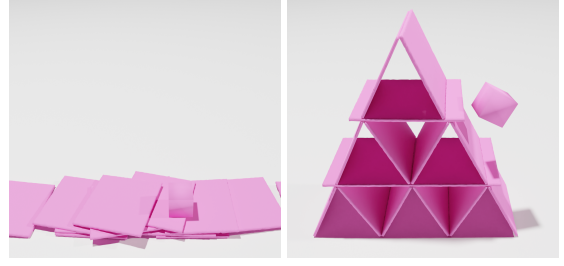


Fig. 20. Stiff card house: we simulate a card house with stiff boards ($E = 0.1\text{GPa}$) and impact the house with a dropping block. Left: the house is fail to keep its shape as we omit the friction between boards. Right: we keep the house shape with frictional contact between the boards.



Fig. 21. Here we show the ability to likewise simulate multiple objects of different codimension simultaneously with frictional contact.

Hence, it remains beneficial to explore more efficient preconditioners in future work for further improvement of the convergence rate.

Our method still uses the friction potential of Li et al. [2020a] with a lagged sliding basis and magnitude of the normal force (refer to our technical supplement for more details). This implies that we suffer from the same limitations that affect accuracy. Specifically, we find that friction-forces are not guaranteed to lie within the local contact plane, which implies that their normal component tends to influence the net barrier force acting in this direction to affect convergence. This can be remedied by using a larger threshold for the friction mollifier (see §5.3 in [Li et al. 2020a]) but this is done to the detriment of static friction accuracy, as larger thresholds induce viscous drag when objects (*i.e.* contact primitives) should be at standstill. These problematic normal friction-force components can likewise be ameliorated by reducing the respective mollifier threshold but this will deteriorate the solver convergence rate. For these reasons, having a friction model that that guarantees strictly in-plane force components with moderate thresholds remains an open problem, which will be meaningful to address in future works.

ACKNOWLEDGMENTS

This work was partially funded by the Research Grant Council of Hong Kong (GRF 17210222). This work was also supported by the Innovation and Technology Commission of the HKSAR Government

under the InnoHK initiative (TransGP project), and the JC STEM Lab of Robotics for Soft Materials funded by The Hong Kong Jockey Club Charities Trust. Finally, we thank the reviewers for their detailed and insightful feedback.

REFERENCES

- J  r  mie Allard, Fran  ois Faure, Hadrien Courtecuisse, Florent Falipou, Christian Duriez, and Paul G Kry. 2010. Volume contact constraints at arbitrary resolution. In *ACM SIGGRAPH 2010 papers*. 1–10.
- Sheldon Andrews, Kenny Erleben, and Zachary Ferguson. 2022. Contact and Friction Simulation for Computer Graphics. In *ACM SIGGRAPH 2022 Courses*. Article 2, 124 pages.
- Ciprian Apetrei. 2014. Fast and Simple Agglomerative LBVH Construction. In *Theory and Practice of Computer Graphics, Leeds, United Kingdom, 2014. Proceedings*, Rita Borgo and Wen Tang (Eds.). Eurographics Association, 41–44.
- David Baraff and Andrew P. Witkin. 1998. Large Steps in Cloth Simulation. In *Proceedings of SIGGRAPH 1998*, Steve Cunningham, Walt Bransford, and Michael F. Cohen (Eds.). ACM, 43–54.
- Robert Bridson, Ronald Fedkiw, and John Anderson. 2002. Robust treatment of collisions, contact and friction for cloth animation. In *Proceedings of the 29th annual conference on Computer graphics and interactive techniques*. 594–603.
- Floyd M. Chitalu, Christophe Dubach, and Taku Komura. 2020. Binary Ostensibly-Implicit Trees for Fast Collision Detection. *Computer Graphics Forum* 39, 2 (2020), 509–521.
- Christer Ericson. 2005. Chapter 6 - Bounding Volume Hierarchies. In *Real-Time Collision Detection*, Christer Ericson (Ed.). Morgan Kaufmann, San Francisco, 235–284.
- Kenny Erleben. 2018. Methodology for assessing mesh-based contact point methods. *ACM Trans. Graph.* 37, 3 (2018), 1–30.
- Yu Fang, Minchen Li, Chenfanfu Jiang, and Danny M. Kaufman. 2021. Guaranteed Globally Injective 3D Deformation Processing. *ACM Trans. Graph. (SIGGRAPH)* 40, 4, Article 75 (2021).
- Zachary Ferguson, Minchen Li, Teseo Schneider, Francisca Gil-Ureta, Timothy Langlois, Chenfanfu Jiang, Denis Zorin, Danny M. Kaufman, and Daniele Panozzo. 2021. Intersection-free Rigid Body Dynamics. *ACM Trans. Graph. (SIGGRAPH)* 40, 4, Article 183 (2021).
- Ming Gao, Xinlei Wang, Kui Wu, Andre Pradhana, Eftychios Sifakis, Cem Yuksel, and Chenfanfu Jiang. 2018. GPU Optimization of Material Point Methods. 37, 6 (2018).
- Ga  l Guennebaud, Beno  t Jacob, et al. 2022. Eigen v3.4. <http://eigen.tuxfamily.org>.
- David Harmon, Etienne Vouga, Rasmus Tamstorf, and Eitan Grinspun. 2008. Robust Treatment of Simultaneous Collisions. *ACM Trans. Graph.* 27, 3 (2008), 1–4.
- Zizhou Huang, Davi Colli Tozoni, Arvi Gjoka, Zachary Ferguson, Teseo Schneider, Daniele Panozzo, and Denis Zorin. 2022. Differentiable solver for time-dependent deformation problems with contact. [arXiv:2205.13643](https://arxiv.org/abs/2205.13643) [cs.GR]
- Geoffrey. Irving, Joseph. Teran, and Ronald Fedkiw. 2004. Invertible Finite Elements for Robust Simulation of Large Deformation. In *Proceedings of the 2004 ACM SIGGRAPH/Eurographics Symposium on Computer Animation (Grenoble, France) (SCA '04)*. Eurographics Association, Goslar, DEU, 131–140.
- Zhongshi Jiang, Scott Schaefer, and Daniele Panozzo. 2017. Simplicial complex augmentation framework for bijective maps. *ACM Trans on Graph* 36, 6 (2017).
- Couro Kane, Jerrold E Marsden, Michael Ortiz, and Matthew West. 2000. Variational integrators and the Newmark algorithm for conservative and dissipative mechanical systems. *International Journal for numerical methods in engineering* 49, 10 (2000), 1295–1325.
- C. Kane, E.A. Repetto, M. Ortiz, and J.E. Marsden. 1999. Finite element analysis of nonsmooth contact. *Computer Methods in Applied Mechanics and Engineering* 180, 1 (1999), 1–26.
- Tero Karras. 2012. Maximizing Parallelism in the Construction of BVHs, Octrees, and k-d Trees. In *Proceedings of HPG 2012*, Carsten Dachsbacher, Jacob Munkberg, and Jacopo Pantaleoni (Eds.). 33–37.
- Danny M Kaufman, Shinjiro Sueda, Doug L James, and Dinesh K Pai. 2008. Staggered projections for frictional contact in multibody systems. In *ACM SIGGRAPH Asia 2008 papers*. 1–11.
- Theodore Kim. 2020. *A Finite Element Formulation of Baraff-Witkin Cloth*. Eurographics Association, Goslar, DEU.
- Theodore Kim, Fernando De Goes, and Hayley Iben. 2019. Anisotropic Elasticity for Inversion-Safety and Element Rehabilitation. *ACM Trans. Graph.* 38, 4, Article 69 (jul 2019), 15 pages.
- Theodore Kim and David Eberle. 2020. Dynamic Deformables: Implementation and Production Practicalities. In *ACM SIGGRAPH 2020 Courses*.
- Tamara G. Kolda and Brett W. Bader. 2009. Tensor Decompositions and Applications. *SIAM Rev.* 51, 3 (September 2009), 455–500.
- Lei Lan, Danny M. Kaufman, Minchen Li, Chenfanfu Jiang, and Yin Yang. 2022a. Affine Body Dynamics: Fast, Stable & Intersection-free Simulation of Stiff Materials. *CoRR abs/2201.10022* (2022). [arXiv:2201.10022](https://arxiv.org/abs/2201.10022)
- Lei Lan, Guanqun Ma, Yin Yang, Changxi Zheng, Minchen Li, and Chenfanfu Jiang. 2022b. Penetration-Free Projective Dynamics on the GPU. *ACM Trans. Graph.* 41, 4, Article 69 (jul 2022), 16 pages.
- Lei Lan, Yin Yang, Danny Kaufman, Junfeng Yao, Minchen Li, and Chenfanfu Jiang. 2021. Medial IPC: Accelerated Incremental Potential Contact with Medial Elastics. *ACM Trans. Graph.* 40, 4, Article 158 (jul 2021), 16 pages.
- Christian Lauterbach, Michael Garland, Shubhabrata Sengupta, David P. Luebke, and Dinesh Manocha. 2009. Fast BVH Construction on GPUs. *Comput. Graph. Forum* 28, 2 (2009), 375–384.
- Christian Lauterbach, Qi Mo, and Dinesh Manocha. 2010. gProximity: hierarchical GPU-based operations for collision and distance queries. In *Computer Graphics Forum*, Vol. 29. Wiley Online Library, 419–428.
- Cheng Li, Min Tang, Ruofeng Tong, Ming Cai, Jieyi Zhao, and Dinesh Manocha. 2020c. P-cloth: interactive complex cloth simulation on multi-gpu systems using dynamic matrix assembly and pipelined implicit integrators. *ACM Trans. Graph.* 39, 6 (2020), 1–15.
- Minchen Li, Zachary Ferguson, Teseo Schneider, Timothy Langlois, Denis Zorin, Daniele Panozzo, Chenfanfu Jiang, and Danny M. Kaufman. 2020a. Incremental Potential Contact: Intersection-and Inversion-Free, Large-Deformation Dynamics. *ACM Trans. Graph.* 39, 4, Article 49 (2020).
- Minchen Li, Zachary Ferguson, Teseo Schneider, Timothy Langlois, Denis Zorin, Daniele Panozzo, Chenfanfu Jiang, and Danny M. Kaufman. 2020b. Technical Supplement to Incremental Potential Contact: Intersection and Inversion-free, Large-Deformation Dynamics. *ACM Trans. Graph.* 39, 4 (2020).
- Minchen Li, Danny M. Kaufman, and Chenfanfu Jiang. 2021. Codimensional Incremental Potential Contact. *ACM Trans. Graph. (SIGGRAPH)* 40, 4, Article 170 (2021).
- Siwang Li, Zherong Pan, Jin Huang, Hujun Bao, and Xiaogang Jin. 2015. Deformable objects collision handling with fast convergence. In *Computer Graphics Forum*, Vol. 34. Wiley Online Library, 269–278.
- Huancheng Lin, Floyd M. Chitalu, and Taku Komura. 2022. Isotropic ARAP Energy Using Cauchy-Green Invariants. *ACM Trans. Graph.* 41, 6, Article 275 (nov 2022), 14 pages.
- Miles Macklin, Kenny Erleben, Matthias M  ller, Nuttapon Chentanez, Stefan Jeschke, and Viktor Makoviyshuk. 2019. Non-Smooth Newton Methods for Deformable Multi-Body Dynamics. *ACM Trans. Graph.* 38, 5, Article 140 (oct 2019), 20 pages.
- Naureen Mahmood, Nima Ghorbani, Nikolaus F. Troje, Gerard Pons-Moll, and Michael J. Black. 2019. AMASS: Archive of Motion Capture as Surface Shapes. In *International Conference on Computer Vision*. 5442–5451.
- Daniel Meister, Shinji Ogaki, Carsten Benthin, Michael J. Doyle, Michael Guthe, and J  ri Bittner. 2021. A Survey on Bounding Volume Hierarchies for Ray Tracing. *Computer Graphics Forum* 40, 2 (2021), 683–712.
- Matthias M  ller, David Charypar, and Markus H. Gross. 2003. Particle-based fluid simulation for interactive applications. In *Proceedings of SCA 2003*. The Eurographics Association, 154–159.
- Matthias M  ller, Nuttapon Chentanez, Tae-Yong Kim, and Miles Macklin. 2015. Air meshes for robust collision handling. *ACM Trans. Graph.* 34, 4 (2015), 1–9.
- Jorge Nocedal and Stephen J. Wright. 2006. *Numerical Optimization* (2nd ed.). Springer, New York, NY, USA.
- Miguel A Otaduy, Rasmus Tamstorf, Denis Steinemann, and Markus Gross. 2009. Implicit contact handling for deformable objects. In *Computer Graphics Forum*, Vol. 28. Wiley Online Library, 559–568.
- Simon Pabst, Artur Koch, and Wolfgang Stra  er. 2010. Fast and scalable cpu/gpu collision detection for rigid and deformable surfaces. In *Computer Graphics Forum*, Vol. 29. Wiley Online Library, 1605–1612.
- Julian Panetta. 2020. Analytic Eigensystems for Isotropic Membrane Energies. <https://doi.org/10.48550/ARXIV.2008.10698>
- Xavier Provot. 1997a. Collision and self-collision handling in cloth model dedicated to design garments. In *Computer Animation and Simulation '97*, Daniel Thalmann and Michiel van de Panne (Eds.). Springer Vienna, Vienna, 177–189.
- Xavier Provot. 1997b. Collision and self-collision handling in cloth model dedicated to design garments. In *Computer Animation and Simulation '97*. Springer, 177–189.
- Alvin Shi and Theodore Kim. 2023. A Unified Analysis of Penalty-Based Collision Energies. *Proc. ACM Comput. Graph. Interact. Tech.* 6, 3, Article 41 (aug 2023), 19 pages.
- Eftychios Sifakis and Jernej Barbic. 2012. FEM Simulation of 3D Deformable Solids: A Practitioner’s Guide to Theory, Discretization and Model Reduction. In *ACM SIGGRAPH 2012 Courses*. Article 20, 50 pages.
- Eftychios Sifakis, Sebastian Marino, and Joseph Teran. 2008. Globally Coupled Collision Handling Using Volume Preserving Impulses. In *Proceedings of Symposium on Computer Animation*.
- Eftychios Sifakis, Igor Neverov, and Ronald Fedkiw. 2005. Automatic Determination of Facial Muscle Activations from Sparse Motion Capture Marker Data. *ACM Trans. Graph.* 24, 3 (jul 2005), 417–425.
- Breannan Smith, Fernando De Goes, and Theodore Kim. 2018. Stable Neo-Hookean Flesh Simulation. *ACM Trans. Graph.* 37, 2, Article 12 (mar 2018), 15 pages.

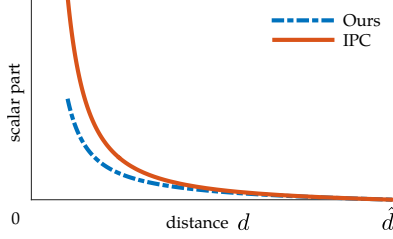


Fig. 22. Comparison with the Gauss-Newton method discussed in [Li et al. 2020a]. We plot the scalar part of the approximate Hessian as a function of distance d .

- Breannan Smith, Fernando De Goes, and Theodore Kim. 2019. Analytic Eigensystems for Isotropic Distortion Energies. *ACM Trans. Graph.* 38, 1, Article 3 (feb 2019), 15 pages.
- Min Tang, Zhongyuan Liu, Ruofeng Tong, and Dinesh Manocha. 2018a. PSCC: Parallel self-collision culling with spatial hashing on GPUs. *Proceedings of the ACM on Computer Graphics and Interactive Techniques* 1, 1 (2018), 1–18.
- Min Tang, Huamin Wang, Le Tang, Ruofeng Tong, and Dinesh Manocha. 2016. CAMA: Contact-aware matrix assembly with unified collision handling for GPU-based cloth simulation. In *Computer Graphics Forum*, Vol. 35. Wiley Online Library, 511–521.
- Min Tang, Tongtong Wang, Zhongyuan Liu, Ruofeng Tong, and Dinesh Manocha. 2018b. I-Cloth: Incremental collision handling for GPU-based interactive cloth simulation. *ACM Trans. Graph.* 37, 6 (2018), 1–10.
- Joseph Teran, Eftychios Sifakis, Geoffrey Irving, and Ronald Fedkiw. 2005. Robust Quasistatic Finite Elements and Flesh Simulation. In *Proceedings of the 2005 ACM SIGGRAPH/Eurographics Symposium on Computer Animation* (Los Angeles, California) (SCA '05). Association for Computing Machinery, New York, NY, USA, 181–190.
- Olivier Tisot. 2019. *Iterative methods for solving linear systems on massively parallel architectures*. Thesis. Sorbonne Université. <https://theses.hal.science/tel-02428348>
- Mickeal Verschoor and Andrei C Jalba. 2019. Efficient and accurate collision response for elastically deformable models. *ACM Trans. Graph.* 38, 2 (2019), 1–20.
- Bolun Wang, Zachary Ferguson, Teso Schneider, Xin Jiang, Marco Attene, and Daniele Panizzo. 2021. A Large-scale Benchmark and an Inclusion-based Algorithm for Continuous Collision Detection. *ACM Trans. Graph.* 40, 5 (2021), 188:1–188:16.
- Huamin Wang. 2021. GPU-based simulation of cloth wrinkles at submillimeter levels. *ACM Trans. Graph.* 40, 4 (2021), 1–14.
- Xinlei Wang, Min Tang, Dinesh Manocha, and Ruofeng Tong. 2018. Efficient BVH-based Collision Detection Scheme with Ordering and Restructuring. *Comput. Graph. Forum* 37, 2 (2018), 227–237.
- Botao Wu, Zhendong Wang, and Huamin Wang. 2022. A GPU-based multilevel additive schwarz preconditioner for cloth and deformable body simulation. *ACM Trans. Graph.* 41, 4 (2022), 1–14.

A GAUSS-NEWTON APPROXIMATION COMPARISON

This section provides a simplified demonstration to show the difference between our Gauss-Newton approximation of the barrier Hessian (cf. § 5.2) and the method discussed in Section 4.3 of [Li et al. 2020a]. We will use the *point-point* test case for the comparison.

Let the determinant (cf. Eq. (9)) be $f = \sqrt{d}$, for the purpose of matching the Euclidean distance based formulation of Li et al. [2020a]. This implies that we have (cf. Eq. (10)) $\mathbf{J} = [\sqrt{d}] \in \mathbb{R}^{1 \times 1}$ from which we can evaluate our gap function as $g = \bar{g} = d$ that we will then substitute into the smoothly-clamped barrier function (cf. Eq. (6)) of Li et al. [2020a] to align our method with this original formulation for comparison.

Revisiting our approximation of the force Jacobian, we have

$$\begin{aligned} \frac{\partial^2 b}{\partial \mathbf{x}^2} &= \frac{\partial \mathbf{J}}{\partial \mathbf{x}} : \frac{\partial^2 b}{\partial \mathbf{J}^2} : \frac{\partial \mathbf{J}}{\partial \mathbf{x}} + \frac{\partial^2 \mathbf{J}}{\partial \mathbf{x}^2} : \frac{\partial b}{\partial \mathbf{J}}, \\ &= \frac{\partial \sqrt{d}}{\partial \mathbf{x}} : \frac{\partial^2 b}{\partial \mathbf{J}^2} : \frac{\partial \sqrt{d}}{\partial \mathbf{x}} \\ &= \frac{1}{2\sqrt{d}} \frac{\partial d}{\partial \mathbf{x}} : \frac{\partial^2 b}{\partial \mathbf{J}^2} : \frac{1}{2\sqrt{d}} \frac{\partial d}{\partial \mathbf{x}}, \\ &= \frac{\partial d}{\partial \mathbf{x}} : \left(\frac{1}{4d} \frac{\partial^2 b}{\partial \mathbf{J}^2} \right) : \frac{\partial d}{\partial \mathbf{x}}, \end{aligned} \quad (37)$$

where the barrier Hessian is given by (cf. Eq. (20))

$$\frac{\partial^2 b}{\partial \mathbf{J}^2} = \left(4g \frac{\partial^2 b}{\partial g^2} + 2 \frac{\partial b}{\partial g} \right) \mathbf{Q}_1 \otimes \mathbf{Q}_1$$

according to our analytic eigensystems.

Since the eigenmatrix $\|\mathbf{Q}_1\|_F^2 = 1$ is normalized, we arrive at the form

$$\begin{aligned} \frac{\partial^2 b}{\partial \mathbf{x}^2} &= \frac{\partial d}{\partial \mathbf{x}} : \left(\frac{1}{4d} \frac{\partial^2 b}{\partial \mathbf{J}^2} \right) : \frac{\partial d}{\partial \mathbf{x}} \\ &= \frac{1}{4d} \left(4g \frac{\partial^2 b}{\partial g^2} + 2 \frac{\partial b}{\partial g} \right) \frac{\partial d}{\partial \mathbf{x}} \otimes \frac{\partial d}{\partial \mathbf{x}} \\ &= \frac{1}{4d} \left(4d \frac{\partial^2 b}{\partial d^2} + 2 \frac{\partial b}{\partial d} \right) \frac{\partial d}{\partial \mathbf{x}} \otimes \frac{\partial d}{\partial \mathbf{x}} \\ &= \left(\frac{\partial^2 b}{\partial d^2} + \frac{1}{2d} \frac{\partial b}{\partial d} \right) \nabla_{\mathbf{x}} d \otimes \nabla_{\mathbf{x}} d, \end{aligned} \quad (38)$$

which resembles the first term in Eq. (22). The primary difference is that Li et al. [2020a]’s proposed Gauss-Newton approximation will only use $\partial^2 b / \partial d^2$ as the scalar part, whereas we use

$$\frac{\partial^2 b}{\partial d^2} + \frac{1}{2d} \frac{\partial b}{\partial d}.$$

A visual comparison is also provided in Fig. 22, which compares the two expressions to reveal that our approximated Hessian produces smaller values than the truncated Hessian proposed in [Li et al. 2020a]. The effect is that our method will produce search directions $\mathbf{d} = (\partial^2 b / \partial \mathbf{x}^2)^{-1} \partial b / \partial \mathbf{x}$ that have larger magnitude. We found that the truncated Hessian of Li et al. [2020a] is effective when simulating soft materials with a relatively large threshold in the iterative solver. However, increasing stiffness (or encountering nearly-parallel *edge-edge* cases) will significantly deteriorate the convergence of this method with potential for failure. In contrast, our proposed analytically projected Gauss-Newton method performs well even under these conditions.

B THE NORMS OF $\frac{\partial b}{\partial \mathbf{x}}$ AND $\frac{\partial^2 b}{\partial \mathbf{x}^2}$

This section is a supplement to Fig. 3, where we present derivations showing the scalar expressions for $\|\partial b / \partial \mathbf{x}\|_2$ and $\|\partial^2 b / \partial \mathbf{x}^2\|_F$ that are used to plot the lines shown.

Expression of the barrier gradient norm. A closed-form expression for the magnitude of the barrier gradient can be obtained directly from Eq. (13), which we rewrite here in vectorized form as

$$\frac{\partial b}{\partial \mathbf{x}} = \frac{\partial b}{\partial g} \text{vec} \left(\frac{\partial \mathbf{J}}{\partial \mathbf{x}} \right) \text{vec} \left(\frac{\partial g}{\partial \mathbf{J}} \right), \quad (39)$$

where the expression for $\partial g/\partial \mathbf{J}$ is given in Eq. (14). Only the terms $\partial b/\partial g$ and $\partial g/\partial \mathbf{J}$ describe the sought magnitude since $\partial \mathbf{J}/\partial \mathbf{x}$ is just a change-of-basis tensor.

Using the expression for the eigenmatrix \mathbf{Q}_1 in Eq. (21), we can rewrite $\partial g/\partial \mathbf{J}$ as

$$\frac{\partial g}{\partial \mathbf{J}} = 2\sqrt{g}\mathbf{Q}_1. \quad (40)$$

Substituting Eq. (40) into Eq. (39), we have

$$\frac{\partial b}{\partial \mathbf{x}} = 2\sqrt{g}\frac{\partial b}{\partial g}\text{vec}\left(\frac{\partial \mathbf{J}}{\partial \mathbf{x}}\right)\text{vec}(\mathbf{Q}_1), \quad (41)$$

to give $-2\sqrt{g}\frac{\partial b}{\partial g} = \|\partial b/\partial \mathbf{x}\|_2$ as the expression for the magnitude of the barrier gradient since the eigenmatrix $\|\mathbf{Q}_1\|_F^2 = 1$ is normalized.

Expression of the barrier force-Jacobian norm. The norm $\|\partial^2 b/\partial \mathbf{x}^2\|_F$ of our approximate barrier force-Jacobian is the primary eigenvalue (Eq. (18)) of the barrier Hessian (Eq. (16)). To show this, we use Eq. (17) by

$$\begin{aligned} \frac{\partial^2 b}{\partial \mathbf{x}^2} &= \text{vec}\left(\frac{\partial \mathbf{J}}{\partial \mathbf{x}}\right)\text{vec}\left(\frac{\partial^2 b}{\partial \mathbf{J}^2}\right)\text{vec}\left(\frac{\partial \mathbf{J}}{\partial \mathbf{x}}\right)^T, \\ &= \text{vec}\left(\frac{\partial \mathbf{J}}{\partial \mathbf{x}}\right)\left(\left(4g\frac{\partial^2 b}{\partial g^2} + 2\frac{\partial b}{\partial g}\right)\text{vec}(\mathbf{Q}_1)\text{vec}(\mathbf{Q}_1)^T\right)\text{vec}\left(\frac{\partial \mathbf{J}}{\partial \mathbf{x}}\right)^T, \\ &= \left(4g\frac{\partial^2 b}{\partial g^2} + 2\frac{\partial b}{\partial g}\right)\text{vec}\left(\frac{\partial \mathbf{J}}{\partial \mathbf{x}}\right)\text{vec}(\mathbf{Q}_1)\text{vec}(\mathbf{Q}_1)^T\text{vec}\left(\frac{\partial \mathbf{J}}{\partial \mathbf{x}}\right)^T, \end{aligned} \quad (42)$$

to give $4g\frac{\partial^2 b}{\partial g^2} + 2\frac{\partial b}{\partial g} = \|\partial^2 b/\partial \mathbf{x}^2\|_F$ as the expression for the norm of our approximate force-Jacobian.

Technical Supplement to “GIPC: Fast and stable Gauss-Newton optimization of IPC barrier energy”

KEMENG HUANG, The University of Hong Kong, TransGP, Hong Kong
 FLOYD M. CHITALU, TransGP, The University of Hong Kong, Hong Kong
 HUANCHENG LIN, TransGP, The University of Hong Kong, Hong Kong
 TAKU KOMURA, The University of Hong Kong, TransGP, Hong Kong

This document provides supplementary details about our derivations and implementation of the main paper. § 1 describes the reference (explicit) constructions of the constraint Jacobian, together with the normal vector. We then use these descriptions to detail our derivations (and simplifications) of the change-of-basis tensor in § 2. We also prove in § 3 that the first eigenvalue (Eq. (18) in the paper) is always positive, and that remaining eigenvalues (Eq. (19) in the paper) are always negative. § 4 describes the intermediate steps we use to arrive at the eigenpairs of our mollified barrier Hessian. In § 5, we provide a summary of the analysis conducted on the friction Hessian, which is followed by supplementary implementation details of our global matrix-free PCG solver in § 6. Supplementary unit test results are provided in § 7. We also provide a comparison of our barrier method and the original formulation on the same hardware (CPU) in § 8. Further supplemental results concerning different linear solvers and the impact of friction-Hessian projection on overall performance are provided in § 9 and § 10, respectively.

CCS Concepts: • **Computing methodologies** → **Physical simulation**; **Collision detection**; **Massively parallel algorithms**.

Additional Key Words and Phrases: IPC, Barrier Hessian, Eigen Analysis, GPU

1 EXPLICITLY CONSTRUCTING JACOBIANS

In this section, we describe the reference method for explicitly computing the constraint Jacobian $J(\mathbf{x}, \hat{d})$ and the normal vector $\mathbf{n}(\mathbf{x})$ for a given contact pair (see also Fig. 1). Several of the constructions we will describe can be found throughout literature (see e.g. [Kane et al. 1999; Müller et al. 2015; Sifakis and Barbic 2012]) but we provide them here for self-containment.

Vertices of a contact pair form a simplex, with which we measure distance d via a matrix $F(\mathbf{x}, \hat{d}) = E(\mathbf{x})\bar{E}(\mathbf{x}, \hat{d})^{-1}$, where the terms defining this F denote the ideal- \bar{E} and current-shape E matrices of the simplex, respectively. In what follows, we will show how to compute E and \bar{E} for each possible simplex/contact-pair.

1.1 Point-triangle

The *point-triangle* case represents a tetrahedron, where the variables constituting the matrix F are

$$E = [\mathbf{x}_2 - \mathbf{x}_1 | \mathbf{x}_3 - \mathbf{x}_1 | \mathbf{x}_4 - \mathbf{x}_1] \in \mathbb{R}^{3 \times 3}$$

$$\bar{E} = [\bar{\mathbf{x}}_2 - \bar{\mathbf{x}}_1 | \bar{\mathbf{x}}_3 - \bar{\mathbf{x}}_1 | \bar{\mathbf{x}}_4 - \bar{\mathbf{x}}_1] \in \mathbb{R}^{3 \times 3}.$$

We construct \bar{E} with

$$\bar{\mathbf{x}}_1 = \mathbf{x}_1 + (\hat{d} - d) \mathbf{n}, \quad \bar{\mathbf{x}}_i = \mathbf{x}_i, \quad i = 2, 3, 4$$

where \mathbf{n} is the triangle normal

$$\mathbf{n} = \frac{(\mathbf{x}_3 - \mathbf{x}_2) \times (\mathbf{x}_4 - \mathbf{x}_2)}{\|(\mathbf{x}_3 - \mathbf{x}_2) \times (\mathbf{x}_4 - \mathbf{x}_2)\|} \in \mathbb{R}^{3 \times 1}, \quad (1)$$

and $d = \mathbf{v} \cdot \mathbf{n}$ is the distance between the point \mathbf{x}_1 and triangle $\mathbf{x}_2, \mathbf{x}_3, \mathbf{x}_4$ using $\mathbf{v} = \mathbf{x}_1 - \mathbf{x}_2$.

1.2 Edge-edge

The *edge-edge* case also represents a tetrahedron, where E and \bar{E} are constructed like the *point-triangle* case. However, the ideal shape positions are now

$$\bar{\mathbf{x}}_1 = \mathbf{x}_1, \quad \bar{\mathbf{x}}_2 = \mathbf{x}_2,$$

$$\bar{\mathbf{x}}_3 = \mathbf{x}_3 + (\hat{d} - d) \mathbf{n}, \quad \bar{\mathbf{x}}_4 = \mathbf{x}_4 + (\hat{d} - d) \mathbf{n},$$

where the normal is computed as in Eq. (1) but using the edge vectors, and with $d = \mathbf{v} \cdot \mathbf{n}$ representing the distance between these edges using $\mathbf{v} = \mathbf{x}_3 - \mathbf{x}_1$.

1.3 Point-edge

The *point-edge* case represents a triangle, with a non-square F constructed with

$$E = [\mathbf{x}_2 - \mathbf{x}_1 | \mathbf{x}_3 - \mathbf{x}_1] \in \mathbb{R}^{3 \times 2}$$

$$\bar{E} = [\bar{\mathbf{x}}_2 - \bar{\mathbf{x}}_1 | \bar{\mathbf{x}}_3 - \bar{\mathbf{x}}_1] \in \mathbb{R}^{2 \times 2},$$

We can compute \bar{E} by projecting vertex components to the plane

$$\bar{\mathbf{x}}_1 = \mathbf{K}\mathbf{H}(\mathbf{x}_1 + (\hat{d} - d) \mathbf{n}_e), \quad \bar{\mathbf{x}}_2 = \mathbf{K}\mathbf{H}\mathbf{x}_2, \quad \bar{\mathbf{x}}_3 = \mathbf{K}\mathbf{H}\mathbf{x}_3,$$

where the in-plane edge normal \mathbf{n}_e ($\mathbf{n}_e \perp \mathbf{x}_2\mathbf{x}_3$) is given by

$$\mathbf{n}_e = \frac{(\mathbf{x}_2 - \mathbf{x}_3) \times \mathbf{n}_t}{\|(\mathbf{x}_1 - \mathbf{x}_2) \times \mathbf{n}_t\|} \in \mathbb{R}^{3 \times 1},$$

with \mathbf{n}_t denoting triangle normal computed as in Eq. (1) but using $\mathbf{x}_1, \mathbf{x}_2$ and \mathbf{x}_3 . The matrix $\mathbf{H} \in \mathbb{R}^{3 \times 3}$ represents a rotation to align the triangle to a canonical axis plane, e.g. with normal $\mathbf{n}_t = (0, 1, 0)$. Several methods exist to determine this rotation with one example being Rodrigues' formula [Murray et al. 1994] from which we get

$$\mathbf{H} = \begin{cases} 2 \frac{(\mathbf{p}+\mathbf{b})(\mathbf{p}+\mathbf{b})^T}{(\mathbf{p}+\mathbf{b})^T(\mathbf{p}+\mathbf{b})} - \mathbf{I} & \mathbf{p} \neq -\mathbf{b} \\ \begin{bmatrix} -1 & 0 & 0 \\ 0 & -1 & 0 \\ 0 & 0 & 1 \end{bmatrix} & \text{otherwise,} \end{cases} \quad (2)$$

Authors' addresses: Kemeng Huang, kmhuang@connect.hku.hk, kmhuang819@gmail.com, The University of Hong Kong, TransGP, Hong Kong; Floyd M. Chitalu, floyd.m.chitalu@gmail.com, TransGP, The University of Hong Kong, Hong Kong; Huancheng Lin, lamws@connect.hku.hk, TransGP, The University of Hong Kong, Hong Kong; Taku Komura, taku@cs.hku.hk, The University of Hong Kong, TransGP, Hong Kong.

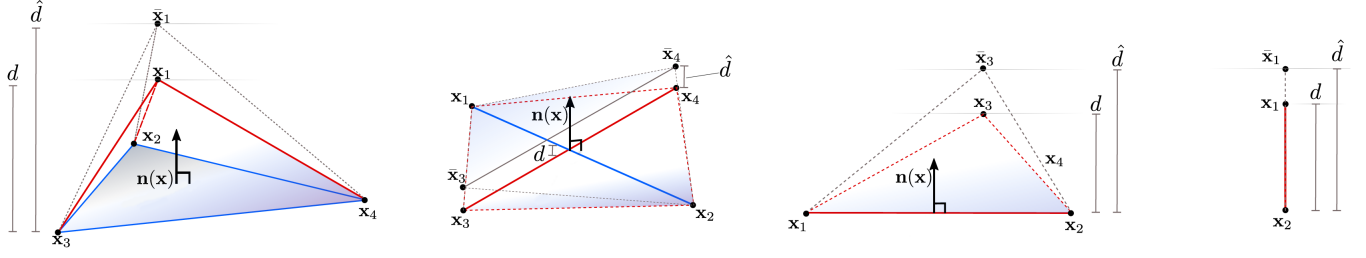


Fig. 1. The primitive contact pairs that are tested for intersection. From left to right, we have point-triangle (tetrahedron); edge-edge (tetrahedron); point-edge (triangle); and point-point (line-segment). In each case, the vertices can be seen as forming a simplex with which we formulate an impermeable barrier energy using a Jacobian (matrix) constructed from these vertices.

where $\mathbf{p} := \mathbf{n}_t$, $\mathbf{b} = [0 \ 1 \ 0]^T$ and $\mathbf{K} \in \mathbb{R}^{2 \times 3}$ is a matrix (subject to our choice of \mathbf{b}) to extract the xz components of a 3D vector

$$\mathbf{K} = \begin{bmatrix} 1 & 0 & 0 \\ 0 & 0 & 1 \end{bmatrix}.$$

Finally, $d = \mathbf{v} \cdot \mathbf{n}_e$ is the distance between point \mathbf{x}_1 and edge $\mathbf{x}_2\mathbf{x}_3$ using $\mathbf{v} = \mathbf{x}_1 - \mathbf{x}_2$.

1.4 Point-Point

The *point-point* case reduces to a line segment and where the Jacobian is a vector. We have

$$\mathbf{E} = \mathbf{v} \in \mathbb{R}^{3 \times 1} \quad \text{and} \quad \bar{\mathbf{E}} = [\bar{\mathbf{x}}_2 - \bar{\mathbf{x}}_1] \in \mathbb{R}, \quad (3)$$

where $\mathbf{v} = \mathbf{x}_2 - \mathbf{x}_1$, and

$$\bar{\mathbf{x}}_1 = \mathbf{KH}(\mathbf{x}_1 + (\hat{d} - d)\mathbf{n}) \in \mathbb{R} \quad \text{and} \quad \bar{\mathbf{x}}_2 = \mathbf{KH}\mathbf{x}_2 \in \mathbb{R},$$

where $\mathbf{n} = \frac{\mathbf{v}}{\|\mathbf{v}\|}$ is the normal, and the rotation \mathbf{H} is constructed similarly to Eq. (2) *i.e.* as one which aligns \mathbf{n} to the canonical y -axis of $(0, 1, 0)$. Assuming the same choice for the vector \mathbf{b} as above, the matrix $\mathbf{K} = [0 \ 1 \ 0]$ now extracts the y -component of a 3D vector. Thus, $d = \mathbf{v} \cdot \mathbf{n} = \|\mathbf{n}\| = \|\mathbf{v}\|$.

In all cases above, we have \mathbf{KHn} as the normal vector used to evaluate the gap function, using \mathbf{n}_e for the point-edge case.

2 CHANGE-OF-BASIS TENSOR

This section outlines how we compute the change-of-basis tensor $\frac{\partial \mathbf{F}}{\partial \mathbf{x}} \in \mathbb{R}^{\text{dims}(\mathbf{F}) \times 3s}$ from a contact pair comprised of s vertices. This tensor can be understood as a column vector with block entries of dimensions $\text{dims}(\mathbf{F}) \equiv \mathbb{R}^{3 \times m}$ for an m -dimensional simplex.

Definition. The general expression defining the change-of-basis tensor is given by

$$\frac{\partial \mathbf{F}}{\partial \mathbf{x}} = \frac{\partial \mathbf{E}}{\partial \mathbf{x}} \bar{\mathbf{E}}^{-1} + \mathbf{E} \frac{\partial \bar{\mathbf{E}}^{-1}}{\partial \mathbf{x}}, \quad (4)$$

where $\bar{\mathbf{E}}(\mathbf{x}(t))$ is our so-called ‘ideal’ configuration matrix which varies unlike the case of hyperelastic materials where the analogous reference shape matrix is constant¹. This variation is evaluated with the identity

$$\frac{\partial \bar{\mathbf{E}}^{-1}}{\partial \mathbf{x}_i} = -\bar{\mathbf{E}}^{-1} \frac{\partial \bar{\mathbf{E}}}{\partial \mathbf{x}_i} \bar{\mathbf{E}}^{-1},$$

¹See also the element rehabilitation scheme of Kim et al. [2019].

and is computed w.r.t the m vertices in the stencil of a contact pair. It is worth noting that the second term $\mathbf{E} \frac{\partial \bar{\mathbf{E}}^{-1}}{\partial \mathbf{x}_i}$ of Eq. (4) has been observed to be negligible during the conducted empirical trials.

Higher order derivatives. The second order derivative $\partial^2 (\bar{\mathbf{E}}^{-1}) / \partial \mathbf{x}^2$ exists too since the analytic expressions of some entries in $\bar{\mathbf{E}}$ are dependent on the normal vector $\mathbf{n}(\mathbf{x})$ that is computed from the cross-product between edge-vectors. This is also the reason why our local force Jacobian (Eq. (15) in the paper) is dependent on $\partial^2 \mathbf{F} / \partial \mathbf{x}^2$ ($\partial^2 \mathbf{J} / \partial \mathbf{x}^2$ in the paper), which intuitively captures higher-order variations in $\bar{\mathbf{E}}$ due to a changing normal vector $\mathbf{n}(\mathbf{x})$ w.r.t positions.

2.1 Relationship between \mathbf{F} and \mathbf{J}

The contact constraint Jacobian $\mathbf{J} \equiv \mathbf{S}$ that we use in the paper can be viewed as corresponding to the stretch factor of the matrix $\mathbf{F} = \mathbf{R}\mathbf{S}$ from polar decomposition². This decomposition yields a rotation \mathbf{R} and symmetric stretch $\mathbf{S} = \mathbf{\Sigma}\mathbf{V}^T$, both of which will be diagonal in our method with $\mathbf{R} = \mathbf{U} = \mathbf{V} = \mathbf{I}$ due to the compressive distortion assumption of the simplex along the vector $-\mathbf{n}(\mathbf{x})$ as outlined in Figure 2 of the paper. In general, either \mathbf{F} or \mathbf{J} can be used to define the barrier function b , its gradient $\partial b / \partial \mathbf{x}$ and force Jacobian $\partial^2 b / \partial \mathbf{x}^2$. The dimensions of the local force vector and force Jacobian matrix will be equal in either case, which can be demonstrated by applying tensor vectorization (*e.g.* on either Eq. (13) or Eq. (15) in the paper) to show that tensor contraction in the derivatives will cancel out differences in the dimensions between \mathbf{F} and \mathbf{J} for a given m -dimensional simplex with $\mathbf{x} \in \mathbb{R}^{3s \times 1}$. The change-of-basis tensor $\partial \mathbf{J} / \partial \mathbf{x}$ is computed w.r.t the explicit entries in the diagonal structure of \mathbf{J} .

3 EIGENVALUE PROPERTIES

This section provides the proof showing that only the first eigenvalue λ_1 (*cf.* Eq. (18) and Eq. (19) in the paper) is ever positive for the standard contact pairs *i.e.* those not representing the nearly-parallel

²It is likewise possible to take the perspective of singular value decomposition $\mathbf{F} = \mathbf{U}\mathbf{\Sigma}\mathbf{V}^T$ from which $\mathbf{J} = \mathbf{\Sigma}$ since the method outlined in the paper may be viewed as working in the local principal stretch space of the deforming simplex along $-\mathbf{n}$.

ALGORITHM 1: Warp reduction for matrix-vector multiplication.

```

for each thread, thread_id do
    /* Variable initialization */
    shared offset;
    H_dims ← m2 // Total entries per Hessian ∈ ℝm×m
    H_id ←  $\frac{\text{thread\_id}}{\text{H\_dims}}$  // Hessian index
    R_id ←  $\frac{\text{thread\_id} \times \text{H\_dims}}{m}$  // Hessian row index
    C_id ← (thread_id % H_dims) % m // Hessian col index
    v_id ←  $\frac{C\_id}{3}$  // Vertex index in Hessian
    vc_id ← C_id % 3 // vertex component index
    e_id ← thread_id % m // Entry index in Hessian row
    h ← load(H_id, R_id, C_id, ...) // Hessian entry value
    // component of vector multiplied with Hessian
    c ← load(v_id, vc_id, ...);
    r ← c · h // scalar multiplication result
    if thread_id == 0 then
        | offset ← (m - e_id);
    end
    /* Wait for 'offset' initialization */
    barrier();
    B_id ←  $\frac{\text{thread\_id} - \text{offset} + m}{m}$  // Hess row index in block
    // Re-calibrated offset of 1st full Hessian row
    l_id ← (thread_id - offset) % m;
    if B_id == 0 then
        | l_id ← thread_id;
    end
    w_id ← thread_id % 32 // Warp index
    // is 1st thread after boundary
    is_boundary ← (l_id == 0) || (w_id == 0);
    // set the bit value of mark according to boundary
    mark ← cudaBrev(cudaBallot(is_boundary));
    // length of reduction range in warp
    interval ← cudaClz(mark « (w_id + 1));
    // clamp to warp size
    interval ← min(interval, 31 - w_id);
    // warp reduction (accumulate 'r')
    iter ← 1;
    while iter < m do
        // read value 'r' of neighbour(s) in warp
        tmp ← cudaShflDown(r, iter);
        if interval ≥ iter then
            | r += tmp
        end
        iter «= 1 // bitshift
    end
    // only 1st thread after boundary will write
    if is_boundary then
        | addToOutputArray(r) // write using atomics
    end
end
    
```

case. We have used Eq. (12) in the main paper to obtain

$$\lambda_1 = \frac{2\hat{d}^4(6g + 2g \ln(g) - 7g^2 - 6g^2 \ln(g) + 1)}{g}, \quad (5)$$

$$\lambda_{2,3} = \frac{-2\hat{d}^4(g-1)(g + 2g \ln(g) - 1)}{g^2}, \quad (6)$$

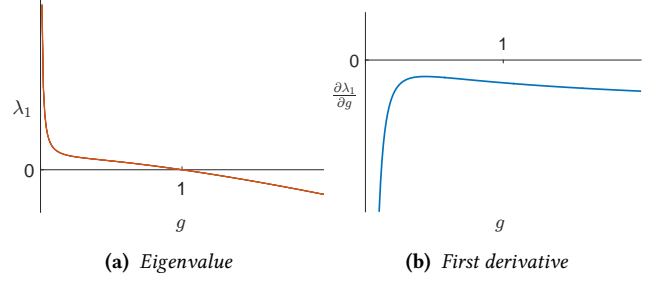


Fig. 2. A plot of Eq. (5) in the paper and its derivatives, where $\hat{d} = 1$.

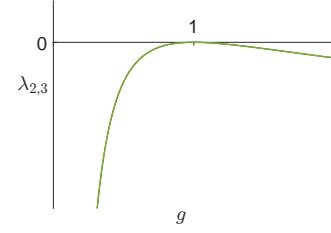


Fig. 3. A plot of Eq. (6) in the paper, where $\hat{d} = 1$.

as the expanded expressions that we use for our proof. We would arrive at different expressions for $\lambda_{1,2,3}$ if we instead used Eq. (24) in the paper but the behaviour (plots) remains the same.

λ_1 is always positive. Since our gap function $g \in (0, 1)$ has limited range, we have

$$\lim_{g \rightarrow 0^+} \lambda_1 = +\infty \quad (7)$$

$$\lim_{g \rightarrow 1} \lambda_1 = 0, \quad (8)$$

where the condition $\lambda_1 \geq 0$ is always true (Fig. 2a).

PROOF. The first eigenvalue λ_1 is monotonically decreasing, which we demonstrate using the 1st derivative of Eq. (5)

$$\frac{\partial \lambda_1}{\partial g} = \frac{-2\hat{d}^4(13g^2 - 2g + 6g^2 \ln(g) + 1)}{g^2}. \quad (9)$$

Eq. (9) is always negative (Fig. 2b) which is inline with our observation in Eq. (8) that λ_1 is ever decreasing from positive to zero as $g \rightarrow 1$. Therefore, $\frac{\partial \lambda_1}{\partial g} < 0$ is always true, which means $\lambda_1 > 0$ is also true when $g \in (0, 1)$. □

$\lambda_{2,3}$ are always negative. The second eigenvalue λ_2 and third eigenvalue λ_3 are always less than zero when $g \in (0, 1)$.

PROOF. Eq. (6) has an odd number of terms which are less-than or equal-to zero

$$\begin{aligned} g - 1 &\leq 0, \\ g + 2g \ln(g) - 1 &\leq 0, \\ -2\hat{d}^4 &\leq 0. \end{aligned} \quad (10)$$

Thus, we have $\lambda_{2,3} \leq 0$, which is also shown in Fig. 3. □

Eq. (7)-Eq. (10) summarise why exactly one eigenpair is sufficient to guarantee positive semi-definiteness for minimizing our barrier energy.

4 APPROXIMATE MOLLIFIED HESSIAN TERMS

This section summarises of the steps to derive Eq. (32) in the paper (§ 4.1), and the steps we follow to arrive at the eigensystem of the last two terms of our mollified barrier Hessian (§ 4.2).

4.1 Eigenvectors of the first two terms

We follow the approach outlined in [Kim et al. 2019], to arrive at the eigenpairs

$$\lambda_{Y1} = 2 \left(\frac{\partial \tilde{b}}{\partial \gamma} + 2\gamma \frac{\partial^2 \tilde{b}}{\partial \gamma^2} \right), \quad \mathbf{Q}_{Y1} = \frac{1}{\sqrt{\gamma}} \mathbf{J} \mathbf{n}_\gamma \mathbf{n}_\gamma^T.$$

where

$$\mathbf{Q}_{Y1} = \frac{1}{\sqrt{c}} \begin{bmatrix} 1 & 0 & 0 \\ 0 & \sqrt{c} & 0 \\ 0 & 0 & f \end{bmatrix} \begin{bmatrix} 0 & 0 & 0 \\ 0 & 1 & 0 \\ 0 & 0 & 0 \end{bmatrix} = \mathbf{n}_\gamma \mathbf{n}_\gamma^T$$

is the expansion from which we get the expression used in the paper. Similar steps are followed to obtain λ_{g1} and $\mathbf{Q}_{g1} = \mathbf{n}_g \mathbf{n}_g^T$.

For the eigenpairs

$$\lambda_{Y2,Y3} = 2 \frac{\partial \tilde{b}}{\partial \gamma}, \quad \mathbf{Q}_{Y2}, \mathbf{Q}_{Y3},$$

we use the twist matrices from Smith et al. [2019]

$$\mathbf{T}_x = \begin{bmatrix} 0 & 0 & 0 \\ 0 & 0 & 1 \\ 0 & -1 & 0 \end{bmatrix}, \quad \mathbf{T}_y = \begin{bmatrix} 0 & 0 & -1 \\ 0 & 0 & 0 \\ 1 & 0 & 0 \end{bmatrix}, \quad \mathbf{T}_z = \begin{bmatrix} 0 & 1 & 0 \\ -1 & 0 & 0 \\ 0 & 0 & 0 \end{bmatrix},$$

to arrive at

$$\mathbf{Q}_{Y2} = \text{normalize}(\mathbf{U} \mathbf{T}_x \Sigma \mathbf{V}^T \mathbf{n}_\gamma \mathbf{n}_\gamma^T), \quad (11)$$

$$\mathbf{Q}_{Y3} = \text{normalize}((\sigma_y \hat{a}_y \mathbf{U} \mathbf{T}_z - \sigma_z \hat{a}_z \mathbf{U} \mathbf{T}_y) \Sigma \mathbf{V}^T \mathbf{n}_\gamma \mathbf{n}_\gamma^T), \quad (12)$$

using SVD $\mathbf{J} = \mathbf{U} \Sigma \mathbf{V}^T$, where $\sigma_{y,z}$ are the second and third singular values from Σ , and $\hat{a}_{y,z}$ are the entries of the vector $\mathbf{V}^T \mathbf{n}_\gamma$. We also have $\mathbf{U} = \mathbf{V} = \mathbf{I}$ due to the special diagonal structure of \mathbf{J} from which \mathbf{Q}_{Y2} and \mathbf{Q}_{Y3} can be simplified as

$$\mathbf{Q}_{Y2} = \begin{bmatrix} 0 & 0 & 0 \\ 0 & 0 & 1 \\ 0 & -1 & 0 \end{bmatrix} \mathbf{n}_\gamma \mathbf{n}_\gamma^T, \quad \mathbf{Q}_{Y3} = \begin{bmatrix} 0 & 1 & 0 \\ -1 & 0 & 0 \\ 0 & 0 & 0 \end{bmatrix} \mathbf{n}_\gamma \mathbf{n}_\gamma^T.$$

Similarly, we can get \mathbf{Q}_{g2} and \mathbf{Q}_{g3} by

$$\mathbf{Q}_{g2} = \begin{bmatrix} 0 & 0 & 0 \\ 0 & 0 & 1 \\ 0 & -1 & 0 \end{bmatrix} \mathbf{n}_g \mathbf{n}_g^T, \quad \mathbf{Q}_{g3} = \begin{bmatrix} 0 & 0 & 1 \\ 0 & 0 & 0 \\ -1 & 0 & 0 \end{bmatrix} \mathbf{n}_g \mathbf{n}_g^T.$$

4.2 Eigenpairs of the last two terms

We arrive at $\lambda_7 \mathbf{Q}_7$ and $\lambda_8 \mathbf{Q}_8$ in the paper with

$$\begin{aligned} \frac{\partial^2 \tilde{b}}{\partial \gamma \partial g} \left(\frac{\partial g}{\partial \mathbf{J}} \otimes \frac{\partial \gamma}{\partial \mathbf{J}} \right) + \frac{\partial^2 \tilde{b}}{\partial g \partial \gamma} \left(\frac{\partial \gamma}{\partial \mathbf{J}} \otimes \frac{\partial g}{\partial \mathbf{J}} \right) = \\ \frac{\partial^2 b}{\partial \gamma \partial g} \mathbf{g}_g \mathbf{g}_\gamma^T + \frac{\partial^2 b}{\partial g \partial \gamma} \mathbf{g}_\gamma \mathbf{g}_g^T = \end{aligned} \quad (13)$$

$$\begin{bmatrix} 0 & 0 & 0 & 0 & 0 & 0 & 0 & 0 & 0 \\ 0 & 0 & 0 & 0 & 0 & 0 & 0 & 0 & 0 \\ 0 & 0 & 0 & 0 & 0 & 0 & 0 & 0 & 0 \\ 0 & 0 & 0 & 0 & 0 & 0 & 0 & 0 & 0 \\ 0 & 0 & 0 & 0 & 0 & 0 & 0 & 0 & 4t \\ 0 & 0 & 0 & 0 & 0 & 0 & 0 & 0 & 0 \\ 0 & 0 & 0 & 0 & 0 & 0 & 0 & 0 & 0 \\ 0 & 0 & 0 & 0 & 0 & 0 & 0 & 0 & 0 \\ 0 & 0 & 0 & 0 & 4t & 0 & 0 & 0 & 0 \end{bmatrix},$$

which is an expansion of the last two terms of the mollified barrier Hessian, where $\mathbf{g}_* = \text{vec}(\partial(*)/\partial \mathbf{J})$ with $*$ being a placeholder for γ or g . We obtain the closed-form expressions of the eigenpairs by analysing this matrix in Eq. (13) as an eigenproblem.

We arrive at our expressions for $\lambda_7' \mathbf{Q}_7'$ and $\lambda_8' \mathbf{Q}_8'$ in the paper by solving an eigenproblem on the auxiliary matrix

$$\begin{aligned} \mathbf{M} = \lambda_{Y1} \text{vec}(\mathbf{Q}_{Y1}) \text{vec}(\mathbf{Q}_{Y1})^T + \lambda_{g1} \text{vec}(\mathbf{Q}_{g1}) \text{vec}(\mathbf{Q}_{g1})^T \\ + \lambda_7 \text{vec}(\mathbf{Q}_7) \text{vec}(\mathbf{Q}_7)^T + \lambda_8 \text{vec}(\mathbf{Q}_8) \text{vec}(\mathbf{Q}_8)^T \end{aligned}$$

$$= \begin{bmatrix} 0 & 0 & 0 & 0 & 0 & 0 & 0 & 0 & 0 \\ 0 & 0 & 0 & 0 & 0 & 0 & 0 & 0 & 0 \\ 0 & 0 & 0 & 0 & 0 & 0 & 0 & 0 & 0 \\ 0 & 0 & 0 & 0 & 0 & 0 & 0 & 0 & 0 \\ 0 & 0 & 0 & 0 & \lambda_{Y1} & 0 & 0 & 0 & 4t \\ 0 & 0 & 0 & 0 & 0 & 0 & 0 & 0 & 0 \\ 0 & 0 & 0 & 0 & 0 & 0 & 0 & 0 & 0 \\ 0 & 0 & 0 & 0 & 0 & 0 & 0 & 0 & 0 \\ 0 & 0 & 0 & 0 & 4t & 0 & 0 & 0 & \lambda_{g1} \end{bmatrix}, \quad (14)$$

based on the fact that the mollified Hessian is defined as

$$\text{vec} \left(\frac{\partial^2 b}{\partial \mathbf{J}^2} \right) \equiv \mathbf{M} + \sum_{i=Y2,Y3,g2,g3} \lambda_i \text{vec}(\mathbf{Q}_i) \text{vec}(\mathbf{Q}_i)^T, \quad (15)$$

The non-orthogonal eigenmatrices \mathbf{Q}_{Y1} , \mathbf{Q}_{g1} , \mathbf{Q}_7 , \mathbf{Q}_8 lie in the subspace represented by \mathbf{Q}_7' and \mathbf{Q}_8' , which we determine by solving an eigenproblem on \mathbf{M} .

5 ANALYSIS OF FRICTION HESSIAN

This section provides a summary of the analysis conducted on the Hessian of the smooth friction model, as proposed by [Li et al. 2020]. The model uses a ‘lagged’ sliding basis, where contact force is computed using some quantities that are computed at the last time step. Specifically, the formulation of the local friction force is

$$F_k(\mathbf{x}, \lambda_k^n, \mathbf{T}_k^n, \mu) = -\mu \lambda_k^n \mathbf{T}_k^n f_1(\|\mathbf{u}_k\|) \frac{\mathbf{u}_k}{\|\mathbf{u}_k\|}, \quad (16)$$

where μ denotes the friction coefficient, k here denotes the collision pair index, $\mathbf{u}_k = \mathbf{T}_k^n \mathbf{x}_k^n \in \mathbb{R}^{2 \times 1}$, \mathbf{x}_k^n is the relative displacement of k -th collision pair, while λ_k^n and $\mathbf{T}_k^n \in \mathbb{R}^{3s \times 2}$ represent the sliding basis and contact normal force derived from the previous time step

that we refer to by the superscript n here. The function denoted here by f_1 will provide a smooth and monotonic transition from 0 to 1 over a finite range

$$f_1(\|\mathbf{u}_k\|) = \begin{cases} -\frac{\|\mathbf{u}_k\|^2}{\epsilon_v^2 \Delta t^2} + \frac{2\|\mathbf{u}_k\|}{\epsilon_v \Delta t}, & \|\mathbf{u}_k\| \in (0, \Delta t \epsilon_v) \\ 1, & \|\mathbf{u}_k\| > \Delta t \epsilon_v \end{cases}, \quad (17)$$

which is also detailed in [Li et al. 2020]. This leads to the corresponding friction potential

$$D_k(\mathbf{x}) = \mu \lambda_k^n f_0(\|\mathbf{u}_k\|). \quad (18)$$

Here, f_0 is defined such that $f'_0 = f_1$ and $f_0(\epsilon_v h) = \epsilon_v \Delta t$ so that $F_k(\mathbf{x}) = -\nabla_{\mathbf{x}} D_k(\mathbf{x})$. The Hessian of $D_k(\mathbf{x})$ can be simply given by:

$$\nabla_{\mathbf{x}}^2 D_k(\mathbf{x}) = \mu \lambda_k^n \mathbf{T}_k^n \left(\frac{f'_1(\|\mathbf{u}_k\|) \|\mathbf{u}_k\| - f_1(\|\mathbf{u}_k\|)}{\|\mathbf{u}_k\|^3} \mathbf{u}_k \mathbf{u}_k^T + \frac{f_1(\|\mathbf{u}_k\|)}{\|\mathbf{u}_k\|} \mathbf{I}_2 \right) \mathbf{T}_k^{nT} \in \mathbb{R}^{3s \times 3s}. \quad (19)$$

where \mathbf{I}_2 is a 2×2 identity matrix. Eigenanalysis of the Hessian in Eq. (19) essentially boils down to the analysis of a simple 2×2 matrix,

$$\frac{f'_1(\|\mathbf{u}_k\|) \|\mathbf{u}_k\| - f_1(\|\mathbf{u}_k\|)}{\|\mathbf{u}_k\|^3} \mathbf{u}_k \mathbf{u}_k^T + \frac{f_1(\|\mathbf{u}_k\|)}{\|\mathbf{u}_k\|} \mathbf{I}_2, \quad (20)$$

which can be accomplished by analytically solving a quadratic characteristic polynomial.

6 DATA-PARALLEL SOLVER

This section provides the high level information (and algorithm) that we use to parallelise our GPU implementation of preconditioned conjugate gradients (PCG) [Shewchuk 1994] without constructing the full system matrix. This scheme has been adopted previously, e.g. by Gao et al. [2018] and Wang et al. [2020], where our novelty lies in the parallel optimization of local matrix-vector multiplications. The remaining vector-vector multiplications of PCG is optimized with the global reduction methods of Zhao et al. [2020].

The traditional approach to solving the global linear system requires prior construction/assembly of a (sparse) system matrix, which involves incrementally *adding* contributions into its block entries from the local Hessians [Baraff and Witkin 1998; Tamstorf et al. 2015]. This is especially suitable for elastic deformation problems with finite elements or mass-spring systems where mesh topology is fixed to allow pre-computation of the non-zero entries/indices in the global matrix. In our case the time-dependent nature of the number of IPC barrier energy terms precludes such pre-computation to affect the cost of book-keeping for tracking dynamically-changing sparse matrix indexing offsets.

Decomposing system matrix-vector multiplication. It is possible to avoid such global construction by decomposing system matrix back to the local form using the distributive property of addition, which we use and can be demonstrated using a simple 2D mass-spring system with three nodes and two springs. Fig. 4 shows two springs

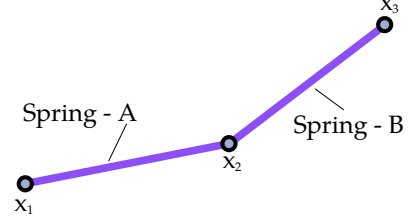


Fig. 4. Mass spring system with two springs

endowed with a (local system) matrix each

$$\mathbf{A} = \begin{bmatrix} \mathbf{A}_{11} & \mathbf{A}_{12} \\ \mathbf{A}_{21} & \mathbf{A}_{22} \end{bmatrix} \equiv \frac{\partial^2 \Psi_A}{\partial \mathbf{x}^2}, \quad (21)$$

$$\mathbf{B} = \begin{bmatrix} \mathbf{B}_{11} & \mathbf{B}_{12} \\ \mathbf{B}_{21} & \mathbf{B}_{22} \end{bmatrix} \equiv \frac{\partial^2 \Psi_B}{\partial \mathbf{x}^2}, \quad (22)$$

which correspond to their energies Ψ_A and Ψ_B , respectively, with block entries $\mathbf{A}_{ij}, \mathbf{B}_{ij} \in \mathbb{R}^{2 \times 2}$. The global system matrix may be constructed as follows:

$$\underbrace{\begin{bmatrix} \mathbf{A}_{11} & \mathbf{A}_{12} & 0 \\ \mathbf{A}_{21} & \mathbf{A}_{22} & 0 \\ 0 & 0 & 0 \end{bmatrix}}_{\mathbf{A}} + \underbrace{\begin{bmatrix} 0 & 0 & 0 \\ 0 & \mathbf{B}_{11} & \mathbf{B}_{12} \\ 0 & \mathbf{B}_{21} & \mathbf{B}_{22} \end{bmatrix}}_{\mathbf{B}} = \underbrace{\begin{bmatrix} \mathbf{A}_{11} & \mathbf{A}_{12} & 0 \\ \mathbf{A}_{21} & \mathbf{A}_{22} + \mathbf{B}_{11} & \mathbf{B}_{12} \\ 0 & \mathbf{B}_{12} & \mathbf{B}_{22} \end{bmatrix}}_{\mathbb{H}},$$

with dimensions $\mathbb{H} \in \mathbb{R}^{6 \times 6}$ which is based on the connectivity of the system.

Two springs sharing one vertex will result in a summation of two specific block entries from \mathbf{A} and \mathbf{B} , which are determined by a local-to-global index map. This map, which is constant, is based on the connectivity of the mass spring system, where ‘local’ refers to node indices in a spring versus the ‘global’ indices in the mass-spring system³. Thus, we have

$$\mathbb{H}\mathbf{c} = (\mathbf{A} + \mathbf{B})\mathbf{c}, \quad = \mathbf{A}\mathbf{c} + \mathbf{B}\mathbf{c} \in \mathbb{R}^{6 \times 1}, \quad (23)$$

with $\mathbf{c} = [\mathbf{c}_1 \quad \mathbf{c}_2 \quad \mathbf{c}_3]^T$ and $\mathbf{c}_i \in \mathbb{R}^{2 \times 1}$ to give

$$\begin{bmatrix} \mathbf{A}_{11}\mathbf{c}_1 + \mathbf{A}_{12}\mathbf{c}_2 \\ \mathbf{A}_{21}\mathbf{c}_1 + (\mathbf{A}_{22} + \mathbf{B}_{11})\mathbf{c}_2 + \mathbf{B}_{12}\mathbf{c}_3 \\ \mathbf{B}_{12}\mathbf{c}_2 + \mathbf{B}_{22}\mathbf{c}_3 \end{bmatrix} = \mathbb{H}\mathbf{c} = \mathbf{c}'.$$

where the vector \mathbf{c} is synonymous with the variable defined in Line (5) of the ‘modified-pcg’ Algorithm of Baraff and Witkin [1998]. The global solution \mathbf{c}' can be decomposed into local solution vectors

$$\begin{bmatrix} \mathbf{A}_{11} & \mathbf{A}_{12} \\ \mathbf{A}_{21} & \mathbf{A}_{22} \end{bmatrix} \begin{bmatrix} \mathbf{c}_1 \\ \mathbf{c}_2 \end{bmatrix} = \begin{bmatrix} \mathbf{A}_{11}\mathbf{c}_1 + \mathbf{A}_{12}\mathbf{c}_2 \\ \mathbf{A}_{21}\mathbf{c}_1 + \mathbf{A}_{22}\mathbf{c}_2 \end{bmatrix} = \mathbf{c}'_{\mathbf{a}} \in \mathbb{R}^{2 \times 1} \quad (24)$$

and

$$\begin{bmatrix} \mathbf{B}_{11} & \mathbf{B}_{12} \\ \mathbf{B}_{21} & \mathbf{B}_{22} \end{bmatrix} \begin{bmatrix} \mathbf{c}_2 \\ \mathbf{c}_3 \end{bmatrix} = \begin{bmatrix} \mathbf{B}_{11}\mathbf{c}_2 + \mathbf{B}_{12}\mathbf{c}_3 \\ \mathbf{B}_{21}\mathbf{c}_2 + \mathbf{B}_{22}\mathbf{c}_3 \end{bmatrix} = \mathbf{c}'_{\mathbf{b}} \in \mathbb{R}^{2 \times 1}. \quad (25)$$

³Note that the same analogy carries through when dealing with contact using our IPC formulation: a collision between two surface boundary elements (e.g. a point and an triangle) will form simplex from which we construct our barrier function, its gradient and Hessian. A vertex will have a local index in the simplex and a global index in the respective mesh(es) in contact.

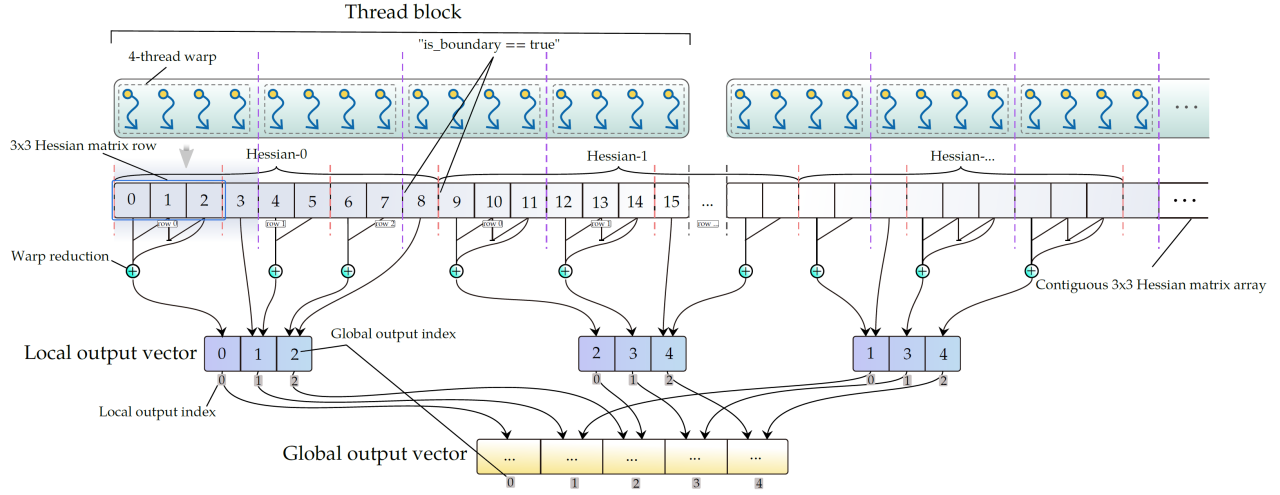


Fig. 5. Warp reduction for parallel dense matrix-vector multiplication (see also Algo. (1)).

to give $\mathbf{c}' = [\mathbf{c}'_{a1} \ (\mathbf{c}'_{a2} + \mathbf{c}'_{b1}) \ \mathbf{c}'_{b2}]^T$ as the basis upon which we build our implementation of the local system matrix-vector multiplications during PCG. So if the local solution vectors \mathbf{c}'_a and \mathbf{c}'_b are computed independently, then it is possible to later merge results into the ‘global’ vector \mathbf{c}' . We use this property to solve the linear system $\mathbb{H}\mathbf{d} = \mathbf{g}$ without ever forming the global system $\mathbb{H}\mathbf{c} = \mathbf{g}$ at each iteration of PCG.

Parallel local matrix-vector multiplication. We assign one thread per scalar entry in a local system matrix (i.e. in \mathbf{A} or in \mathbf{B}), and apply a CUDA-warp level reduction scheme (Algo. (1)) to compute the components of the local solution vector (i.e. \mathbf{c}'_a or \mathbf{c}'_b) in parallel. Briefly, threads in a warp are each mapped to one scalar entry in a local system matrix; the thread will then multiply the matrix entry to the corresponding component of the input vector \mathbf{c} . The multiplication result is then stored in private register memory, which (using CUDA builtins `c1z`, `shfl`down etc.) is then accumulated within each warp before being added to the global output vector \mathbf{c}' .

However, the inconsistency between the CUDA thread block size (can only be 2^n , where $n > 4$) and the local Hessian dimension ($3n \times 3n$, where $n = 4, 3, 2$), as well as the warp size (32), unavoidably results in a challenge for executing the process of multiplying the matrix-vector elements and summing them in parallel. Ideally, the elements of the same row of Hessian are managed by the same thread warp, as then the summation of the matrix-vector elements can be done by warp reduction, which is significantly faster than summing the product individually by atomic operations. As shown in Fig. 5, the inconsistent sizes of the thread block/thread warp/matrix dimensions easily cause each row/matrix to be managed across different thread blocks/warps.

To maximize parallelism, we define a data structure that represents the size and range of reduction in each row of the matrix, which consists of the start position and the length of the reduction. For example, in Fig. 5, in the first row of Hessian-0, the start position is 0, and the length is 3, while in the second row the start position is

4 and the length is 2. We can maximize the parallelism and minimize the branching, such that approximately one thread per row (of any local system matrix) will actually commit data to the global memory (see Algo. (1) for the details).

The local system matrices from our IPC formulation will at-most have dimensions $\mathbb{R}^{12 \times 12}$ but allocating such space for all of our contact pairs (potentially millions) is wasteful since some pairs require much less memory (e.g. *point-point* with $\mathbb{R}^{6 \times 6}$). Thus, we also arrange these matrices into four storage buffers based on the *type* of contact pairs to minimize storage costs and improve parallelism by grouping workloads with same Hessian dimensions. In addition, we also design the warp reduction scheme (Algo. (1)) to assume that all local system matrices assigned to each block/group of CUDA threads have the same local system matrix dimensions to reduce book-keeping and minimize divergent execution flow.

7 SUPPLEMENTARY UNIT TESTS

This section provides supplementary results, which show additional units tests that were used to evaluate our implementation. These results are shown in Fig. 6 and Fig. 7. Readers are also referred to our supplementary video.

8 COMPARISON OF BARRIER METHODS ON CPU

Different aspects of implementation such as hardware choice (e.g. GPU or CPU) and the choice of linear solver will inevitably influence the performance enhancements observed in our barrier method. Thus, to validate the accuracy of the improvements described in the paper, we conduct additional evaluations of our barrier method within the CPU-IPC framework. This involved implementing our barrier method in CPU-IPC while using the same direct solver, CHOLMOD, to measure performance improvement. The purpose of this evaluation was to demonstrate improvements across various time steps and material stiffness parameter settings. The detailed experimental settings and the corresponding evaluation results are provided in Tab. 5, which shows the improvements of our method as described

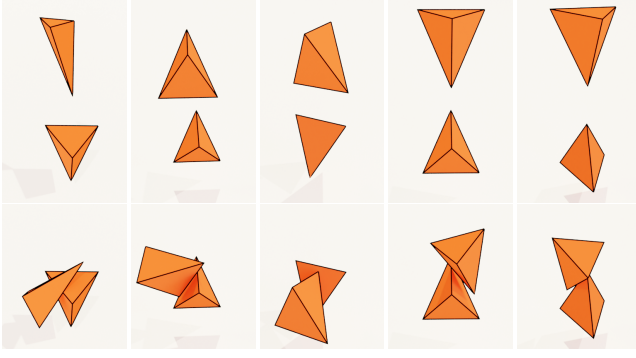


Fig. 6. Unit tests: From left to right we have the point-triangle, edge-edge, parallel edge-edge, point-edge and point-point case. We robustly pass all these tests.

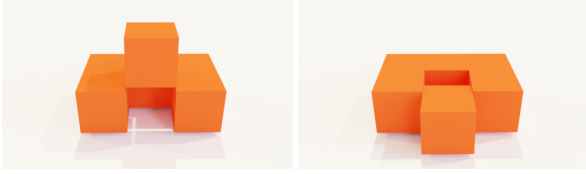


Fig. 7. Aligned, close and nonsmooth contact test: conforming collisions are also accurately and stably resolved.

in the paper (see column #1). Our method leads to a consistently lower number of Newton iterations on average. The advantage of our approach is most evident when simulating with highly stiff materials, reducing the number of iterations by up-to 3 \times .

Table 1. Solution tolerance versus the number of Newton iterations, and the gradient-norm at convergence.

	1e-2	1e-3	1e-4	1e-5	1e-6	1e-7
Iterations	3159	5772	9300	11123	14474	16631
Gradient-norm	3e-2	3e-3	3e-4	3e-5	3e-6	3e-7

Table 2. Newton Iterations w.r.t the gradient-norm tolerance in standard CPU-IPC [Li et al. 2020].

	3e-2	3e-3	3e-4	3e-5	3e-6	3e-7
Iterations	3582	6292	9765	11910	15105	16962

9 COMPARISON BETWEEN DIRECT SOLVER AND PCG

In this section, we present and discuss results based on an apple-to-apple comparison between the direct solver and PCG method in terms of Newton solver iterations, tested with the scene shown in Fig. (10 (a)) in the paper. This experiment is based on the setup

Table 3. Newton iterations w.r.t PCG tolerance and Newton tolerance (based on gradient-norm). The data is plotted in Fig. 8.

PCG Tolerance	Newton solver tolerance (gradient-norm)					
	3e-2	3e-3	3e-3	3e-5	3e-6	3e-7
1e-1	3981	7058	10418	13726	14970	19021
1e-2	3894	6585	10573	13257	15213	18534
1e-3	3698	6381	10340	12747	15915	18651
1e-4	3557	6116	10051	12163	14508	17367
1e-5	3846	6344	9896	12075	15320	17454
1e-6	3766	6288	9068	12695	14414	17491
1e-7	3666	6235	9921	12059	15120	17222

Table 4. Newton Iterations w.r.t the gradient-norm tolerance, using our barrier method (with mollification) implemented the CPU-IPC framework.

	3e-2	3e-3	3e-4	3e-5	3e-6	3e-7
Iterations	2322	5425	8280	11231	14407	16148

described in § 8, using our PCG method within the CPU-IPC framework [Li et al. 2020]. The objective is to illustrate that the PCG tolerance employed in our experiments (*i.e.* to give $\delta_{new} < 1e-4\delta_0$ as the termination condition of PCG), as mentioned in the paper, is sufficient for generating simulations of comparable accuracy to those achieved with direct solver in CPU-IPC.

In Tab. 1 and Tab. 2, we provide reference data showing the number of Newton iterations w.r.t tolerance, where this tolerance is defined based on the solution and the gradient, respectively. We obtain this data by running standard CPU-IPC [Li et al. 2020] with a direct solver (CHOLMOD) in two phases. In the first phase, we run with six distinct settings of the solution tolerance and record the number of Newton iterations and gradient-norm at convergence. We then repeat the simulation in the second phase using the recorded gradient-norm as the solver tolerance to analyse the number of iterations required to converge. The solution threshold with the highest accuracy in our experimental setup is approximately 1e-7 m/s. The gathered data in Tab. 1 and Tab. 2 is used as reference to compare against the results shown in Tab. 3. It is important to note that the convergence condition is determined by $\frac{\|d\|_\infty}{I\Delta t} \leq \epsilon_d$ for the solution tolerance and $\frac{\|g\|_\infty}{I\Delta t^2} \leq \epsilon_g$ for the gradient tolerance.

In Tab. 3, we provide the data we obtain by running standard CPU-IPC with PCG instead of a direct solver, which we use to demonstrate that CPU-IPC converges to the same accuracy with either of these two linear solvers. The gradient-norm is used for determining whether the Newton solver has converged in this experiment, which we do in order to ensure a fair comparison because using the solution for validation may be less reliable given that it varies with different linear solvers (potentially impacting convergence/Newton iterations). Crucially, the data of Tab. 3 and Fig. 8 provide further evidence that our choice of solution tolerance (1e-4) for PCG in

	v, t, f	ρ, E, ν	\hat{d}, ϵ_d	μ, ϵ_v	$\Delta t, \# \Delta t$	buildCP		buildGH		solve		CCD		#i		misc		timeTot		speedup (cpu-Our vs. cpu-Li)
						cpu-Li	cpu-Our	cpu-Li	cpu-Our	cpu-Li	cpu-Our	cpu-Li	cpu-Our	cpu-Li	cpu-Our	cpu-Li	cpu-Our	cpu-Li	cpu-Our	
Fig. (10)(paper)	32k, 135k, 38k	1e3, 1e4, 0.49 1e3, 1e5, 0.49 1e3, 1e6, 0.49 1e3, 1e7, 0.49	1e-3, 1e-2	-	0.01, 95	6.33e2	4.39e2	2.97e2	1.95e2	3.39e3	2.68e3	5.41e2	3.75e2	33.2	24.4	1.93e1	1.61e1	4.88e3	3.71e3	1.32×
					0.01, 80	4.09e2	2.34e2	2.05e2	1.08e2	2.32e3	1.51e3	3.58e2	2.07e2	26.5	16.5	1.81e1	1.30e1	3.31e3	2.07e3	1.60×
					0.01, 100	4.66e2	2.27e2	2.39e2	1.01e2	2.74e3	1.42e3	4.04e2	2.27e2	24.8	12.7	2.14e1	1.25e1	3.87e3	1.99e3	1.94×
					0.01, 81	4.62e2	1.44e2	2.33e2	6.28e1	2.62e3	8.76e2	3.94e2	1.23e2	29.8	9.93	3.11e1	1.10e1	3.74e3	1.22e3	3.06×
Fig. (14)(paper)	8k, 36k, 10k(dolphin) 30k, -, 60k(funnel)	1e3, 1e4, 0.40	1e-3, 1e-2	-	0.01, 300	2.64e3	2.35e3	5.47e2	2.16e2	3.46e3	3.10e3	2.06e3	1.75e3	22.7	20.1	1.84e2	1.67e2	8.89e3	7.58e3	1.15×
					0.02, 150	1.62e3	1.25e3	4.27e2	1.52e2	2.55e3	1.92e3	1.36e3	1.03e3	29.6	23.2	1.03e2	8.68e1	6.06e3	4.45e3	1.36×
					0.03, 100	1.24e3	9.50e2	3.62e2	1.44e2	2.13e3	1.69e3	1.09e3	8.47e2	36.8	28.4	6.82e1	5.68e1	4.89e3	3.69e3	1.32×
					0.04, 75	9.69e2	7.18e2	3.28e2	1.16e2	1.72e3	1.29e3	8.93e2	6.96e2	38.4	28.6	5.38e1	4.41e1	3.97e3	2.87e3	1.38×
					0.05, 60	8.86e2	6.55e2	3.13e2	1.21e2	1.59e3	1.24e3	8.28e2	6.88e2	43.6	32.7	4.47e1	3.63e1	3.66e3	2.74e3	1.33×

Table 5. Performance summary using comparison Li et al. [2020]. The columns are as follows: number of vertices, including the interior for tetrahedral meshes (v); number of tetrahedra (t); number of surface triangles (f); time step size in seconds (Δt); material density(ρ), Young’s modulus (E) in units of pascals Pa, and Poisson’s ratio (ν); computational accuracy target in meters (\hat{d}) which is set w.r.t. to the scene bounding box diagonal length l ; Newton Solver tolerance threshold (ϵ_d); friction coefficient (μ) and velocity magnitude bound (ϵ_v); Total number of time steps ($\# \Delta t$); Total time to build/find contact pairs (buildCP); Total time to build energy gradients and Hessians for all types (buildGH); Total linear solver time (solve); Total CCD time (CCD); Average number of Newton iterations per time step ($\#i$); Total time for remaining miscellaneous tasks (misc); Total simulation compute time (timeTot); We replace the barrier method of CPU-IPC (Li et al. [2020]) with ours to estimate the speedup of our method. All time measurements are presented in seconds.

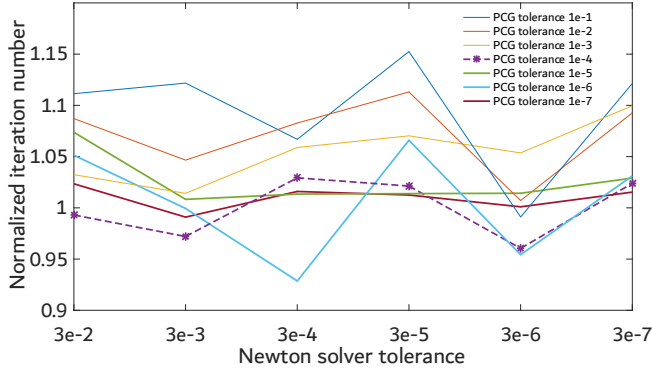


Fig. 8. Normalized plot of the rows in Tab. 3: Newton-iteration number when using PCG w.r.t tolerance. We normalize by the corresponding iteration number for the direct solver (cf. Tab. 2). The figure demonstrates that the difference in Newton-iteration number between using PCG and the direct solver is typically within a margin of approximately 5% when PCG tolerance is smaller than $1e-4$. Using a higher accuracy tolerance for PCG does not necessarily lower the Newton-iteration count, as locally accurate solutions (i.e. per Newton iteration) do not necessarily translate into a globally optimal convergence rate. Our data further indicates that even with a relatively low-accuracy PCG tolerance, the Newton solver can still converge. This follows the fact that PCG provides an optimal search direction and step size within the current Krylov subspace, which corresponds to the direction of energy descent in that subspace, even with a relatively low-accuracy tolerance.

the paper yields an equivalent number of Newton iterations when compared to higher-accuracy thresholds.

In order to demonstrate that our barrier method, using the PCG solver with $1e-4$ tolerance, maintains the accuracy of the IPC method, we conducted additional tests. We replaced the barrier method with our approach and continued to use the gradient-norm threshold to assess the convergence capability of our method across different simulation accuracies. The results, presented in Tab. 4, indicate

that our barrier method is capable of performing high-accuracy simulations as well.

10 IMPACT OF FRICTION HESSIAN PROJECTION

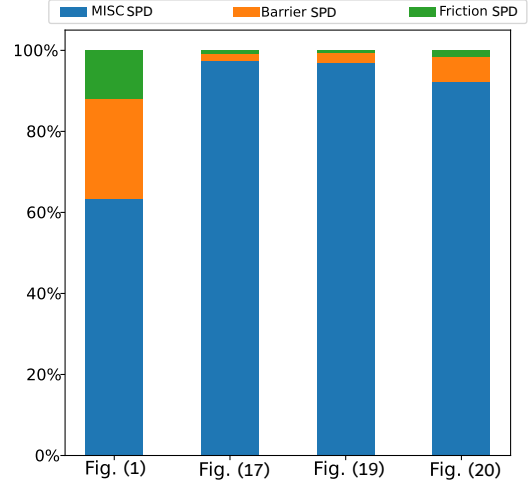


Fig. 9. Percentage of time on Hessian projection: Time breakdown considering the local Hessian projections in our simulator, which include those of the elastic energy. Here we particularly focus on projections for friction- and barrier Hessians. The x-axis refers to the figures/demos provided in the paper, which are the examples involving friction (full simulation).

Fig. 9 provides a comprehensive breakdown of compute time between local friction- and barrier Hessian projection alongside the remaining miscellaneous local projections that take place in our simulator (e.g. elastic energy Hessian). The results show that projection of the friction hessian has negligible overhead when compared to our approximated analytic barrier Hessian projection. We have found friction Hessian projection to merely require one-third to one-half the time needed to compute barrier Hessian projection.

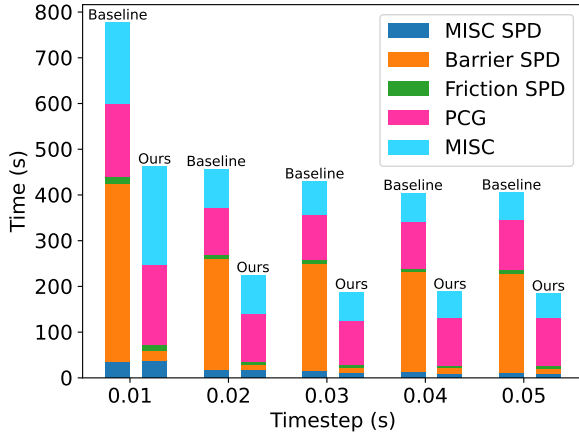


Fig. 10. By employing the Funnel test showcased in Fig. (14) and conducting the comparison illustrated in Fig. (9) of the main paper with friction added, we include a time breakdown of the friction- and barrier Hessian projections, along with the remaining miscellaneous components of our simulator.

To provide a deeper understanding of the role friction plays within large-scale contact simulations, we also run a duplicate experiment of the demo shown in Fig. (14) of the paper, setting the friction coefficient to $1e-2$ (i.e. μ parameter in Tab. 5 or Tab. (5) in the paper). A breakdown w.r.t total simulation time is presented in Fig. 10, where it can be observed that the time expenditure associated with friction Hessian projection has overall minimal footprint.

REFERENCES

- David Baraff and Andrew P. Witkin. 1998. Large Steps in Cloth Simulation. In *Proceedings of SIGGRAPH 1998*, Steve Cunningham, Walt Bransford, and Michael F. Cohen (Eds.). ACM, 43–54.
- Ming Gao, Xinlei Wang, Kui Wu, Andre Pradhana, Eftychios Sifakis, Cem Yuksel, and Chenfanfu Jiang. 2018. GPU Optimization of Material Point Methods. 37, 6 (2018).
- C. Kane, E.A. Repetto, M. Ortiz, and J.E. Marsden. 1999. Finite element analysis of nonsmooth contact. *Computer Methods in Applied Mechanics and Engineering* 180, 1 (1999), 1–26.
- Theodore Kim, Fernando De Goes, and Hayley Iben. 2019. Anisotropic Elasticity for Inversion-Safety and Element Rehabilitation. *ACM Trans. Graph.* 38, 4, Article 69 (jul 2019), 15 pages.
- Minchen Li, Zachary Ferguson, Teseo Schneider, Timothy Langlois, Denis Zorin, Daniele Panozzo, Chenfanfu Jiang, and Danny M. Kaufman. 2020. Incremental Potential Contact: Intersection-and Inversion-Free, Large-Deformation Dynamics. *ACM Trans. Graph.* 39, 4, Article 49 (2020).
- Matthias Müller, Nuttapon Chentanez, Tae-Yong Kim, and Miles Macklin. 2015. Air meshes for robust collision handling. *ACM Trans. Graph.* 34, 4 (2015), 1–9.
- Richard M. Murray, S. Shankar Sastry, and Li Zexiang. 1994. *A Mathematical Introduction to Robotic Manipulation* (1st ed.). CRC Press, Inc., USA.
- Jonathan R Shewchuk. 1994. *An Introduction to the Conjugate Gradient Method Without the Agonizing Pain*. Technical Report. USA.
- Eftychios Sifakis and Jernej Barbic. 2012. FEM Simulation of 3D Deformable Solids: A Practitioner’s Guide to Theory, Discretization and Model Reduction. In *ACM SIGGRAPH 2012 Courses*. Article 20, 50 pages.
- Breannan Smith, Fernando De Goes, and Theodore Kim. 2019. Analytic Eigensystems for Isotropic Distortion Energies. *ACM Trans. Graph.* 38, 1, Article 3 (feb 2019), 15 pages.
- Rasmus Tamstorf, Toby Jones, and Stephen F. McCormick. 2015. Smoothed Aggregation Multigrid for Cloth Simulation. *ACM Trans. Graph.* 34, 6, Article 245 (oct 2015), 13 pages.

Xinlei Wang, Minchen Li, Yu Fang, Xinxin Zhang, Ming Gao, Min Tang, Danny M. Kaufman, and Chenfanfu Jiang. 2020. Hierarchical Optimization Time Integration for CFL-Rate MPM Stepping. *ACM Trans. Graph.* 39, 3, Article 21 (apr 2020), 16 pages.

Zipeng Zhao, Kemeng Huang, Chen Li, Changbo Wang, and Hong Qin. 2020. A Novel Plastic Phase-Field Method for Ductile Fracture with GPU Optimization. *Comput. Graph. Forum* 39, 7 (2020), 105–117.